



<b>Publication Year</b>	2023
<b>Acceptance in OA</b>	2025-03-03T13:09:57Z
<b>Title</b>	CEERS Key Paper. I. An Early Look into the First 500 Myr of Galaxy Formation with JWST
<b>Authors</b>	Finkelstein, Steven L., Bagley, Micaela B., Ferguson, Henry C., Wilkins, Stephen M., Kartaltepe, Jeyhan S., Papovich, Casey, Yung, L. Y. Aaron, Haro, Pablo Arrabal, Behroozi, Peter, DICKINSON, MARK, Kocevski, Dale D., Koekemoer, Anton M., Larson, Rebecca L., Le Bail, Aurélien, Morales, Alexa M., Pérez-González, Pablo G., Burgarella, Denis, Davé, Romeel, HIRSCHMANN, Michaela Monika, Somerville, Rachel S., Wuyts, Stijn, Bromm, Volker, Casey, Caitlin M., FONTANA, Adriano, Fujimoto, Seiji, Gardner, Jonathan P., Giavalisco, Mauro, GRAZIAN, Andrea, Grogin, Norman A., Hathi, Nimish P., Hutchison, Taylor A., Jha, Saurabh W., Jogee, Shardha, Kewley, Lisa J., Kirkpatrick, Allison, Long, Arianna S., Lotz, Jennifer M., PENTERICCI, Laura, Pierel, Justin D.R., Pirzkal, Nor, Ravindranath, Swara, Ryan, Russell E., Trump, Jonathan R., Yang, Guang, Bhatwdekar, Rachana, BISIGELLO, Laura, Buat, Véronique, CALABRO', Antonello, CASTELLANO, Marco, Cleri, Nikko J., Cooper, M. C., Croton, Darren, Daddi, Emanuele, Dekel, Avishai, Elbaz, David, Franco, Maximilien, Gawiser, Eric, Holwerda, Benne W., Huertas-Company, Marc, Jaskot, Anne E., Leung, Gene C.K., Lucas, Ray A., Mobasher, Bahram, Pandya, Viraj, Tacchella, Sandro, Weiner, Benjamin J., Zavala, Jorge A.
<b>Publisher's version (DOI)</b>	10.3847/2041-8213/acade4
<b>Handle</b>	<a href="http://hdl.handle.net/20.500.12386/36377">http://hdl.handle.net/20.500.12386/36377</a>
<b>Journal</b>	THE ASTROPHYSICAL JOURNAL LETTERS
<b>Volume</b>	946



# CEERS Key Paper. I. An Early Look into the First 500 Myr of Galaxy Formation with JWST

Steven L. Finkelstein<sup>1</sup>, Micaela B. Bagley<sup>1</sup>, Henry C. Ferguson<sup>2</sup>, Stephen M. Wilkins<sup>3,4</sup>, Jeyhan S. Kartaltepe<sup>5</sup>, Casey Papovich<sup>6,7</sup>, L. Y. Aaron Yung<sup>8,55</sup>, Pablo Arrabal Haro<sup>9</sup>, Peter Behroozi<sup>10,11</sup>, Mark Dickinson<sup>9</sup>, Dale D. Kocevski<sup>12</sup>, Anton M. Koekemoer<sup>13</sup>, Rebecca L. Larson<sup>1,14</sup>, Aurélien Le Bail<sup>15</sup>, Alexa M. Morales<sup>1</sup>, Pablo G. Pérez-González<sup>16</sup>, Denis Burgarella<sup>17</sup>, Romeel Davé<sup>18,19</sup>, Michaela Hirschmann<sup>20,21</sup>, Rachel S. Somerville<sup>22</sup>, Stijn Wuyts<sup>23</sup>, Volker Bromm<sup>1</sup>, Caitlin M. Casey<sup>1</sup>, Adriano Fontana<sup>24</sup>, Seiji Fujimoto<sup>1,25,26,56</sup>, Jonathan P. Gardner<sup>27</sup>, Mauro Giavalisco<sup>28</sup>, Andrea Grazian<sup>29</sup>, Norman A. Grogin<sup>2</sup>, Nimish P. Hathi<sup>2</sup>, Taylor A. Hutchison<sup>8,55</sup>, Saurabh W. Jha<sup>30</sup>, Shardha Jogee<sup>1</sup>, Lisa J. Kewley<sup>31</sup>, Allison Kirkpatrick<sup>32</sup>, Arianna S. Long<sup>1,56</sup>, Jennifer M. Lotz<sup>33</sup>, Laura Pentericci<sup>24</sup>, Justin D. R. Pierel<sup>2</sup>, Nor Pirzkal<sup>2,34</sup>, Swara Ravindranath<sup>2</sup>, Russell E. Ryan, Jr.<sup>2</sup>, Jonathan R. Trump<sup>35</sup>, Guang Yang<sup>36,37</sup>, Rachana Bhatawdekar<sup>38</sup>, Laura Bisigello<sup>29,39</sup>, Véronique Buat<sup>17</sup>, Antonello Calabrò<sup>24</sup>, Marco Castellano<sup>24</sup>, Nikko J. Cleri<sup>6,7</sup>, M. C. Cooper<sup>40</sup>, Darren Croton<sup>41,42</sup>, Emanuele Daddi<sup>15</sup>, Avishai Dekel<sup>43</sup>, David Elbaz<sup>15</sup>, Maximilien Franco<sup>1</sup>, Eric Gawiser<sup>30</sup>, Benne W. Holwerda<sup>44</sup>, Marc Huertas-Company<sup>45,46,47</sup>, Anne E. Jaskot<sup>48</sup>, Gene C. K. Leung<sup>1</sup>, Ray A. Lucas<sup>13</sup>, Bahram Mobasher<sup>49</sup>, Viraj Pandya<sup>50,56</sup>, Sandro Tacchella<sup>51,52</sup>, Benjamin J. Weiner<sup>53</sup>, and Jorge A. Zavala<sup>54</sup>

<sup>1</sup> Department of Astronomy, The University of Texas at Austin, Austin, TX, USA<sup>2</sup> Space Telescope Science Institute, Baltimore, MD, USA<sup>3</sup> Astronomy Centre, University of Sussex, Falmer, Brighton BN1 9QH, UK<sup>4</sup> Institute of Space Sciences and Astronomy, University of Malta, Msida MSD 2080, Malta<sup>5</sup> Laboratory for Multiwavelength Astrophysics, School of Physics and Astronomy, Rochester Institute of Technology, 84 Lomb Memorial Drive, Rochester, NY 14623, USA<sup>6</sup> Department of Physics and Astronomy, Texas A&M University, College Station, TX 77843-4242, USA<sup>7</sup> George P. and Cynthia Woods Mitchell Institute for Fundamental Physics and Astronomy, Texas A&M University, College Station, TX 77843-4242, USA<sup>8</sup> Astrophysics Science Division, NASA Goddard Space Flight Center, 8800 Greenbelt Road, Greenbelt, MD 20771, USA<sup>9</sup> NSF's National Optical-Infrared Astronomy Research Laboratory, 950 North Cherry Avenue, Tucson, AZ 85719, USA<sup>10</sup> Department of Astronomy and Steward Observatory, University of Arizona, Tucson, AZ 85721, USA<sup>11</sup> Division of Science, National Astronomical Observatory of Japan, 2-21-1 Osawa, Mitaka, Tokyo 181-8588, Japan<sup>12</sup> Department of Physics and Astronomy, Colby College, Waterville, ME 04901, USA<sup>13</sup> Space Telescope Science Institute, 3700 San Martin Drive, Baltimore, MD 21218, USA<sup>14</sup> NSF Graduate Fellow<sup>15</sup> Université Paris-Saclay, Université Paris Cité, CEA, CNRS, AIM, F-91191, Gif-sur-Yvette, France<sup>16</sup> Centro de Astrobiología (CAB), CSIC-INTA, Ctra. de Ajalvir km 4, Torrejón de Ardoz, E-28850, Madrid, Spain<sup>17</sup> Aix Marseille Univ, CNRS, CNES, LAM Marseille, France<sup>18</sup> Institute for Astronomy, University of Edinburgh, Blackford Hill, Edinburgh, EH9 3HJ, UK<sup>19</sup> Department of Physics and Astronomy, University of the Western Cape, Robert Sobukwe Road, Bellville, Cape Town 7535, South Africa<sup>20</sup> Institute of Physics, Laboratory of Galaxy Evolution, Ecole Polytechnique Fédérale de Lausanne (EPFL), Observatoire de Sauverny, 1290 Versoix, Switzerland<sup>21</sup> INAF-Osservatorio Astronomico di Trieste, Via Tiepolo 11, I-34131 Trieste, Italy<sup>22</sup> Center for Computational Astrophysics, Flatiron Institute, 162 5th Avenue, New York, NY 10010, USA<sup>23</sup> Department of Physics, University of Bath, Claverton Down, Bath BA2 7AY, UK<sup>24</sup> INAF-Osservatorio Astronomico di Roma, via di Frascati 33, I-00078 Monte Porzio Catone, Italy<sup>25</sup> Cosmic Dawn Center (DAWN), Jagtvej 128, DK-2200 Copenhagen N, Denmark<sup>26</sup> Niels Bohr Institute, University of Copenhagen, Lyngbyvej 2, DK-2100 Copenhagen Ø, Denmark<sup>27</sup> Astrophysics Science Division, Goddard Space Flight Center, Code 665, Greenbelt, MD 20771, USA<sup>28</sup> University of Massachusetts Amherst, 710 North Pleasant Street, Amherst, MA 01003-9305, USA<sup>29</sup> INAF-Osservatorio Astronomico di Padova, Vicolo dell'Osservatorio 5, I-35122, Padova, Italy<sup>30</sup> Department of Physics and Astronomy, Rutgers, the State University of New Jersey, Piscataway, NJ 08854, USA<sup>31</sup> Center for Astrophysics, Harvard & Smithsonian, 60 Garden Street, Cambridge, MA 02138, USA<sup>32</sup> Department of Physics and Astronomy, University of Kansas, Lawrence, KS 66045, USA<sup>33</sup> Gemini Observatory/NSF's National Optical-Infrared Astronomy Research Laboratory, 950 North Cherry Avenue, Tucson, AZ 85719, USA<sup>34</sup> ESA/AURA, STScI, 3700 San Martin Drive, MD 21218, USA<sup>35</sup> Department of Physics, University of Connecticut, 196 Auditorium Road, Unit 3046, Storrs, CT 06269, USA<sup>36</sup> Kapteyn Astronomical Institute, University of Groningen, P.O. Box 800, 9700 AV Groningen, The Netherlands<sup>37</sup> SRON Netherlands Institute for Space Research, Postbus 800, 9700 AV Groningen, The Netherlands<sup>38</sup> European Space Agency, ESA/ESTEC, Keplerlaan 1, 2201 AZ Noordwijk, The Netherlands<sup>39</sup> Dipartimento di Fisica e Astronomia "G. Galilei," Università di Padova, Via Marzolo 8, I-35131 Padova, Italy<sup>40</sup> Department of Physics & Astronomy, University of California, Irvine, 4129 Reines Hall, Irvine, CA 92697, USA<sup>41</sup> Centre for Astrophysics & Supercomputing, Swinburne University of Technology, Hawthorn, VIC 3122, Australia<sup>42</sup> ARC Centre of Excellence for All Sky Astrophysics in 3 Dimensions (ASTRO 3D), Australia<sup>43</sup> Racah Institute of Physics, The Hebrew University of Jerusalem, Jerusalem 91904, Israel<sup>44</sup> Physics & Astronomy Department, University of Louisville, Louisville, KY 40292, USA<sup>45</sup> Instituto de Astrofísica de Canarias, La Laguna, Tenerife, Spain<sup>46</sup> Universidad de la Laguna, La Laguna, Tenerife, Spain<sup>47</sup> Université Paris-Cité, LERMA—Observatoire de Paris, PSL, Paris, France<sup>48</sup> Department of Astronomy, Williams College, Williamstown, MA 01267, USA<sup>49</sup> Department of Physics and Astronomy, University of California, 900 University Avenue, Riverside, CA 92521, USA<sup>50</sup> Columbia Astrophysics Laboratory, Columbia University, 550 West 120th Street, New York, NY 10027, USA<sup>51</sup> Kavli Institute for Cosmology, University of Cambridge, Madingley Road, Cambridge, CB3 0HA, UK

<sup>52</sup> Cavendish Laboratory, University of Cambridge, 19 JJ Thomson Avenue, Cambridge, CB3 0HE, UK  
<sup>53</sup> MMT/Steward Observatory, University of Arizona, 933 North Cherry Avenue, Tucson, AZ 85721, USA

<sup>54</sup> National Astronomical Observatory of Japan, 2-21-1 Osawa, Mitaka, Tokyo 181-8588, Japan

Received 2022 November 10; revised 2022 December 15; accepted 2022 December 22; published 2023 March 27

## Abstract

We present an investigation into the first 500 Myr of galaxy evolution from the Cosmic Evolution Early Release Science (CEERS) survey. CEERS, one of 13 JWST ERS programs, targets galaxy formation from  $z \sim 0.5$  to  $>10$  using several imaging and spectroscopic modes. We make use of the first epoch of CEERS NIRC*am* imaging, spanning  $35.5 \text{ arcmin}^2$ , to search for candidate galaxies at  $z > 9$ . Following a detailed data reduction process implementing several custom steps to produce high-quality reduced images, we perform multiband photometry across seven NIRC*am* broad- and medium-band (and six Hubble broadband) filters focusing on robust colors and accurate total fluxes. We measure photometric redshifts and devise a robust set of selection criteria to identify a sample of 26 galaxy candidates at  $z \sim 9\text{--}16$ . These objects are compact with a median half-light radius of  $\sim 0.5 \text{ kpc}$ . We present an early estimate of the  $z \sim 11$  rest-frame ultraviolet (UV) luminosity function, finding that the number density of galaxies at  $M_{\text{UV}} \sim -20$  appears to evolve very little from  $z \sim 9$  to 11. We also find that the abundance (surface density [ $\text{arcmin}^{-2}$ ]) of our candidates exceeds nearly all theoretical predictions. We explore potential implications, including that at  $z > 10$ , star formation may be dominated by top-heavy initial mass functions, which would result in an increased ratio of UV light per unit halo mass, though a complete lack of dust attenuation and/or changing star formation physics may also play a role. While spectroscopic confirmation of these sources is urgently required, our results suggest that the deeper views to come with JWST should yield prolific samples of ultrahigh-redshift galaxies with which to further explore these conclusions.

*Unified Astronomy Thesaurus concepts:* [Early universe \(435\)](#); [Galaxy formation \(595\)](#); [Galaxy evolution \(594\)](#); [High-redshift galaxies \(734\)](#)

## 1. Introduction

The epoch of reionization marks the period when energetic photons (presumably from massive stars in early galaxies; e.g., Stark 2016; Finkelstein et al. 2019; Robertson 2022) ionized the gas in the intergalactic medium (IGM). Understanding when and how this process occurs is crucial to constraining both the earliest phases of galaxy formation (which kick-started this process) and how the evolution of the IGM temperature affects the star formation efficiency in low-mass halos throughout (and after) this transition.

Advances in deep near-infrared (near-IR) imaging with the Hubble Space Telescope (HST) have pushed constraints on galaxy evolution into the first billion years after the Big Bang. Studies of public blank-field surveys including the Hubble Ultra Deep Field (HUDF; Beckwith et al. 2006; Bouwens et al. 2010; Oesch et al. 2010), the Cosmic Assembly Near-infrared Deep Extragalactic Legacy Survey (CANDELS; Grogin et al. 2011; Koekemoer et al. 2011), the Hubble Frontier Fields (HFF; Lotz et al. 2017), and the Brightest of Reionizing Galaxy survey (Trenti et al. 2011) have uncovered thousands of galaxies at  $z > 6$  (e.g., Bouwens et al. 2015, 2022a; Finkelstein et al. 2015, 2022a; Ishigaki et al. 2015; McLeod et al. 2016; Morishita et al. 2018; Oesch et al. 2018; Bridge et al. 2019; Rojas-Ruiz et al. 2020; Bagley et al. 2022a). The evolution of the rest-frame ultraviolet (UV) luminosity function has been well studied to  $z \sim 8$  (e.g., Bouwens et al. 2015; Finkelstein et al. 2015), with some constraints placed at  $z \sim 9$  and 10 (e.g., Oesch et al. 2018; Bouwens et al. 2019; Bagley et al. 2022a;

Finkelstein et al. 2022a). However, little was known about the  $z > 10$  universe prior to JWST beyond the unexpected discovery of an exceptionally bright  $z = 10.957$  galaxy (Oesch et al. 2016; Jiang et al. 2021). This knowledge gap is due to the modest light-gathering power of the 2.4 m HST and the fact that at  $z > 10$ , galaxies become one-band (F160W; HST/WFC3's reddest filter) detections. Rest-UV emission from galaxies completely redshifts out of HST observability at  $z \gtrsim 12.5$ .

This has left a major gap in our knowledge of galaxy formation at early times. Do galaxies form stars fairly inefficiently, like our own Milky Way, and build up slowly? Or is star formation in the early universe more rapid due to high gas densities and frequent interactions? Equally exciting and unknown, does the initial mass function (IMF) begin to show signs of evolution? Models predict that top-heavy IMFs should dominate at very low metallicities (e.g., Bromm & Larson 2004), so observations should begin to see such signatures. Answering these questions about the physical processes dominating the earliest star formation requires detailed observations of the earliest galaxies to form in our universe, and JWST was designed to push our cosmic horizons to the highest redshifts. The  $7\times$  larger light-gathering power combined with the large field of view and near-IR sensitivity of NIRC*am* (Rieke et al. 2005) sets the stage for major advances in our ability to study early galaxy formation. Cycle 1 of JWST includes several programs encompassing hundreds of hours that all have the early universe as their primary science goal.

Indeed, in just the days to weeks after the first science data were released, several papers were submitted discussing not only the detection of objects at the expected redshifts of  $z \sim 10\text{--}11$  (e.g., Adams et al. 2022; Castellano et al. 2022; Labbe et al. 2022; Naidu et al. 2022b; Whittler et al. 2023) but some candidates at  $z \sim 12\text{--}17$  (e.g., Donnan et al. 2023, hereafter D23; Finkelstein et al. 2022b; Harikane et al. 2023).

<sup>55</sup> NASA Postdoctoral Fellow.

<sup>56</sup> NASA Hubble Fellow.



Original content from this work may be used under the terms of the [Creative Commons Attribution 4.0 licence](#). Any further distribution of this work must maintain attribution to the author(s) and the title of the work, journal citation and DOI.

The existence of galaxies at such early times, and especially at such bright magnitudes for some sources, could potentially challenge early models of galaxy formation (e.g., Boylan-Kolchin 2022; Ferrara et al. 2022; Mason et al. 2023). However, these studies originally relied on very early photometric calibration; subsequent calibration data shifted the photometric zero-points significantly (Boyer et al. 2022). Now that the flux calibration and overall data reduction pipeline has stabilized, it is prudent to take a detailed look at what constraints we can place on this early epoch.

Here we use the first epoch of data from the Cosmic Evolution Early Release Science (CEERS; survey description to come in S. Finkelstein et al. 2022, in preparation) survey. CEERS was designed in part to provide our earliest detailed glimpse into the  $z > 10$  universe, and these CEERS data were among the first Cycle 1 science exposures taken, included in the first publicly released data on 2022 July 14. We search these data for  $z \gtrsim 9$  galaxy candidates, heretofore difficult (if not impossible) to find with HST. We place an emphasis on building a robust sample via a detailed photometric cataloging process coupled with stringent selection criteria, both backed by simulations. Section 2 describes the observations and data reduction, while Section 3 describes our photometry and photometric redshift measurements, and Section 4 discusses our sample selection procedure. We describe our sample in Section 5 and present a comparison to other early samples in Section 6. In Section 7, we present the  $z \sim 11$  UV luminosity function and the cumulative surface density of early galaxies, and we discuss implications on the physics dominating galaxy formation at the earliest times in Section 8. We summarize our results and present our conclusions in Section 9. In this paper, we assume the latest Planck flat  $\Lambda$ CDM cosmology with  $H_0 = 67.36 \text{ km s}^{-1} \text{ Mpc}^{-1}$ ,  $\Omega_m = 0.3153$ , and  $\Omega_\Lambda = 0.6847$  (Planck Collaboration et al. 2020). All magnitudes are in the absolute bolometric (AB) system (Oke & Gunn 1983).

## 2. Data

CEERS is one of 13 early release science surveys designed to obtain data covering several scientific themes of astronomy early in Cycle 1, along with testing out multiple instrument modes and providing early public data to the community. CEERS consists of a mosaic of 10 NIRCcam pointings in the CANDELS Extended Groth Strip (EGS) field, with six obtained in parallel with prime NIRSpec observations and four in parallel with prime MIRI observations (four of these pointings also include NIRCcam wide-field slitless grism spectroscopy). Here we use imaging data from NIRCcam obtained during the first epoch of CEERS, during 2022 June 21–22. This consists of short-wavelength (SW) and long-wavelength (LW) images in both NIRCcam A and B modules taken over four pointings, labeled NIRCcam1, NIRCcam2, NIRCcam3, and NIRCcam6. Each pointing was observed with seven filters: F115W, F150W, and F200W on the SW side and F277W, F356W, F410M, and F444W on the LW side.

### 2.1. Data Reduction

The NIRCcam images used here are those released with the first CEERS public data release (Data Release 0.5), which are fully described in Bagley et al. (2022b). Here we briefly highlight the key features of the data reduction, directing the reader to Bagley et al. (2022b) for more details.

We reduce the raw NIRCcam imaging through version 1.7.2 of the JWST Calibration Pipeline, with custom modifications designed to correct for additional features in the data. We use the calibration reference file context<sup>57</sup> pipeline mapping (pmap) 0989. We begin by running stage 1 of the calibration pipeline, which performs detector-level corrections and outputs a count-rate image in units of counts per second, adopting all default parameters for this stage. We then perform custom corrections to flag and remove snowballs from all exposures, subtract off the large-scale wisps in F150W and F200W using wisp templates created by the NIRCcam team, and measure and remove  $1/f$  noise via a median measured (amplifier by amplifier) along rows and columns. The images are then flat-fielded and flux-calibrated using stage 2 of the calibration pipeline, again adopting the default values, to produce images in units of MJy  $\text{sr}^{-1}$ . The pmap 0989 reference files include ground flats that have been corrected for illumination gradients measured with in-flight data and improved but still preliminary photometric calibration reference files. We find that the flux calibration does a good job of synchronizing the zero-points across the NIRCcam detectors (to within the 2%–5% level; Bagley et al. 2022b) but that an additional absolute flux calibration may be required at the few percent level (see Section 3.6). These flat and photometric calibration reference files will continue to be improved and updated throughout Cycle 1.

We align the images using a custom version of the TweakReg routine, which is designed to register an image to an absolute world coordinate system frame by matching sources detected in each image with those in a reference catalog. Our modified version of the routine uses SEXTRACTOR (hereafter SE; Bertin & Arnouts 1996) to measure source centroids in each individual image. We then align each image to a reference catalog constructed from an HST F160W mosaic with astrometry tied to Gaia EDR3 (see Section 2.2 and Koekemoer et al. 2011, for details on the methods used for the mosaic construction). We first align images from the same detector but different dithers to each other, allowing for shifts in  $x$  and  $y$  and achieving an rms of  $\sim 3\text{--}6 \text{ mas source}^{-1}$  for this relative alignment. We next align all images to the F160W reference image, allowing  $xy$  shifts and rotations in the SW images and an additional scaling factor to account for large-scale distortions in the LW images. The rms of this absolute alignment is  $\sim 12\text{--}15$  and  $\sim 5\text{--}10 \text{ mas}$  when comparing WFC3 to NIRCcam and NIRCcam to NIRCcam, respectively. We note that we followed a slightly different procedure for NIRCcam3, aligning F277W to HST/WFC3 F160W and then using F277W as the new reference for all other NIRCcam filters. This altered procedure was required to address additional offsets registered in one portion of the F160W image in this region (see Bagley et al. 2022b, for details).

Finally, we create mosaics for each pointing in all filters in the following way. We subtract a pedestal value off of each individual image and scale the read-noise variance maps such that they include an estimate of the robustly measured sky variance. The mosaics are then created using the Resample routine in stage 3 of the calibration pipeline, which uses the drizzle algorithm with an inverse variance weighting (Casertano et al. 2000; Fruchter & Hook 2002). We drizzle the images to an output pixel scale of  $0.03 \text{ pixel}^{-1}$  and use the

<sup>57</sup> [jwst-crds.stsci.edu](http://jwst-crds.stsci.edu), pmap 0989 corresponds to NIRCcam instrument mapping 0232.

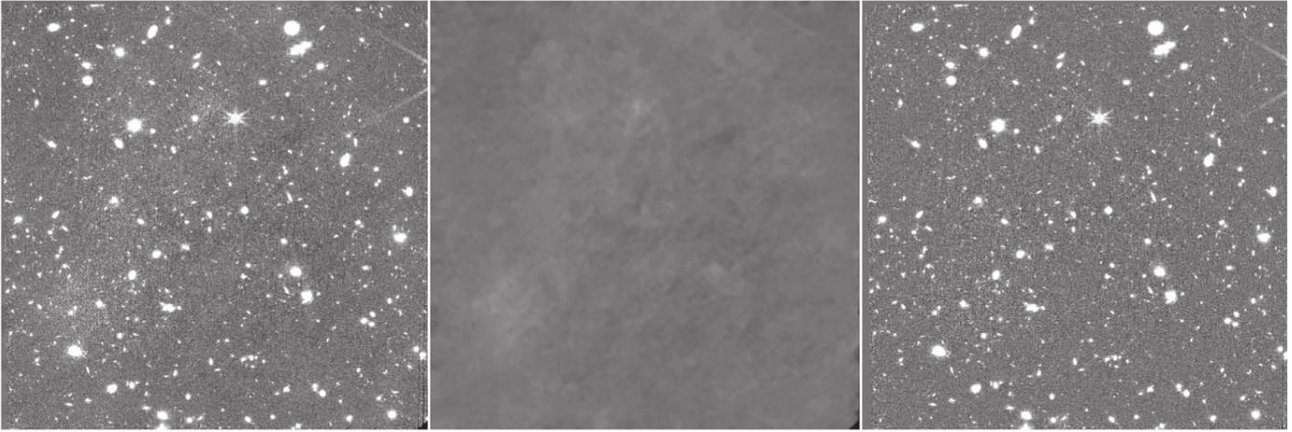


**Figure 1.** Example of the results of our background-subtraction procedure. The left panel shows a zoom-in on the science image of the ALONG module of our F444W mosaic in the CEERS1 pointing. The middle panel is the derived background, and the right panel is the background-subtracted science image. By progressively masking out objects in smaller tiers, this method is able to capture both small- and large-scale fluctuations. The full details of this process are available in Bagley et al. (2022b).

same tangent point as that of the HST mosaics, such that the images in all filters, NIRC1 and HST, are pixel-aligned.

### 2.2. HST Imaging Data

The EGS field has archival HST imaging from the All-wavelength Extended Groth Strip International Survey (AEGIS; Davis et al. 2007), CANDELS (Grogin et al. 2011; Koekemoer et al. 2011), 3D-HST (Momcheva et al. 2016), and various follow-up programs. The entire CEERS field is covered by F606W, F814W, F125W, (shallow 800 s) F140W, and F160W; portions are covered by F105W. For CEERS, we produced an updated version (v1.9) of the CANDELS EGS mosaics,<sup>58</sup> specifically aligning their astrometry onto Gaia DR3 and on the same 30 mas pixel scale as our NIRC1 images. In each of the HST mosaics, we create smaller cutouts to match the footprints of the drizzled NIRC1 mosaics in each pointing. In this way, we have pixel-aligned imaging in 12–13 filters per field (NIRC1 does not include F105W coverage) from  $\sim 0.5$  to  $5 \mu\text{m}$ .

## 3. Photometry

In this section, we describe the creation of our HST+JWST catalog. As the focus is on high-redshift galaxies, this catalog is optimized for faint, compact sources. To ensure accurate photometric redshifts, significant attention is paid to calculation of accurate colors and uncertainties.

### 3.1. Background Subtraction

The procedure adopted to remove background nonuniformities is described in detail by Bagley et al. (2022b). Briefly, it involves several different tiers of source masking aimed at removing large-scale structures—including the wings of bright, extended galaxies—while preserving small-scale structures (including the wings of faint galaxies). We have found this procedure to be more effective than the built-in background-subtraction procedure in SE, and we therefore use these images as inputs to SE (Section 3.3) and disable its background-

subtraction step. We show an example of our background subtraction results in Figure 1.

### 3.2. Point-spread Function Matching

The FWHM of the NIRC1 point-spread function (PSF) varies significantly across the wavelengths of the filters used. As the selection of high-redshift galaxies depends on our ability to measure accurate colors, ensuring that a similar fraction of light is measured in all bands is crucial. In this work, we accomplish this by matching the PSFs in our images to the F444W filter, as it is the reddest filter and thus has the largest PSF ( $\text{FWHM} = 0''.161$ ).

Our procedure for PSF matching follows Finkelstein et al. (2022a), which we summarize here. In each filter, we create a preliminary photometric catalog made using SE v2.25.0 (Bertin & Arnouts 1996) and identify potential PSF stars by searching for the stellar locus in a plane of half-light radius versus source magnitude (making custom cuts in both quantities for each filter). We excluded objects with neighbors within 50 pixels with magnitudes brighter than the magnitude of the star in question minus 1. As stars were more difficult to identify in some bands (e.g., F115W and the shallower F410M), we combined stars identified in the SW and LW channel bands to one list for each channel, which typically resulted in 10–20 stars per NIRC1 pointing. We then visually inspected each star in each image, removing stars near detector edges, with other defects, or with close neighbors not excluded by the previous cut to generate one star list per filter per pointing.

The PSFs were then generated by stacking stars that passed this inspection. As our observations in all four pointings utilized the same dither pattern and were taken at a similar time, we create one PSF per filter by stacking all stars over all four pointings, increasing the signal-to-noise ratio (S/N) of our PSF. For each star, we extract a  $101 \times 101$  pixel box, upsample by a factor of 10, measure the centroid, and shift the star to be centered in this upsampled image. We then downsample back to the native resolution, rotate the star by a random position angle (to account for situations when the position angle of the observations was not identical), and normalize the star’s peak flux to unity. The final PSF was made by median-combining

<sup>58</sup> <https://ceers.github.io/releases.html#hdr1>

**Table 1**  
Imaging Data Summary

Camera	Filter	FWHM	PSF Enclosed Flux ( $d = 0''.2$ )	Point-source Limiting Magnitude ( $5\sigma$ )	Zero-point Correction
JWST/NIRCam SW	F115W	$0''.066$	0.80	29.2	$1.07 \pm 0.03$
JWST/NIRCam SW	F150W	$0''.070$	0.80	29.0	$1.05 \pm 0.02$
JWST/NIRCam SW	F200W	$0''.077$	0.76	29.2	$1.03 \pm 0.03$
JWST/NIRCam LW	F277W	$0''.123$	0.64	29.2	$1.00 \pm 0.03$
JWST/NIRCam LW	F356W	$0''.142$	0.58	29.2	$1.01 \pm 0.02$
JWST/NIRCam LW	F410M	$0''.155$	0.56	28.4	$1.00 \pm 0.02$
JWST/NIRCam LW	F444W	$0''.161$	0.52	28.6	$0.99 \pm 0.02$
HST/ACS	F606W	$0''.118$	0.70	28.6	$1.02 \pm 0.02$
HST/ACS	F814W	$0''.124$	0.63	28.3	$0.96 \pm 0.03$
HST/WFC3	F105W	$0''.235$	0.35	27.1	$0.97 \pm 0.04$
HST/WFC3	F125W	$0''.244$	0.33	27.3	$0.95 \pm 0.03$
HST/WFC3	F140W	$0''.247$	0.32	26.7	$0.95 \pm 0.03$
HST/WFC3	F160W	$0''.254$	0.30	27.4	$0.95 \pm 0.03$

**Note.** The PSFs were created by stacking stars across all four pointings. For our photometry, we PSF match all filters with FWHM smaller than the F444W PSF FWHM to the F444W PSF. We note that the HST imaging used is on the same 30 mas pixel scale, which affects the FWHM of the PSF. The limiting magnitude is that measured in a  $0''.2$  diameter aperture on the unmatched images, corrected to a total based on the PSF flux enclosed in that aperture size, averaged over the four fields. The derived corrections to the photometric zero-points for each filter were derived using the best-fitting EAZY models to  $\sim 900$  galaxies with secure spectroscopic redshifts. These corrections are due to a combination of residual differences between our estimated total fluxes and true total fluxes, differences between the model templates and true galaxies, and true photometric zero-point inaccuracies (using the photometric reference files from pmap 0989 for NIRCam). Because these corrections depend specifically on our photometry procedure, they may not be appropriate for other photometric catalogs.

the individual stars. The final PSFs have a centroiding accuracy of  $\sim 0.05$ – $0.1$  pixels.

Kernels to match bluer PSFs to F444W were created with the PYPHER Python routine<sup>59</sup> (Boucaud et al. 2016), and these bluer images were then convolved with their respective kernels. We included the HST/ACS F606W and F814W imaging in this PSF-matching process, as their PSF FWHMs are smaller than that of F444W. However, the HST/WFC3-band PSF FWHMs are larger than F444W, so we do not convolve these images. This will necessitate a correction accounting for the lower fraction of flux encompassed in a given aperture in these filters, which we discuss in Section 3.3.1.

We tested our PSF-matching process by measuring curves of growth of the PSF stars in the images. We find that the median enclosed flux at an aperture diameter of  $0''.3$  was within 5% (and often less) of the F444W value for all filters (while prior to this PSF-matching process, the bluer filter measurements encompassed  $\sim 20\%$  more light at this radius). We provide the median FWHM values in each filter in Table 1.

### 3.3. Source Extraction

We use SE in two-image mode to measure accurate photometry for each of our four pointings. It requires a detection image to identify sources. We elect to use the inverse variance-weighted sum of the PSF-matched F277W and F356W images as our detection image to better detect faint sources. We do not include F200W in this stack, as the Ly $\alpha$  break enters this filter at  $z = 13.4$ , and we do not wish to bias our catalog against extreme-redshift galaxies (the blue edge of F277W corresponds to a Ly $\alpha$  break redshift of  $z = 18.9$ ), while the inclusion of F444W could have potentially begun to bias against very blue sources.

Using this detection image, we run SE cycling through the seven NIRCam images and six HST images as the

measurement image. The key source detection parameters were initially optimized using the CEERS simulated imaging<sup>60</sup> (Bagley et al. 2022b) and further tweaked by inspecting their performance on the final mosaics. The parameters we used best recovered faint sources while minimizing contamination by spurious objects. These key parameters were DETECT\_THRESH = 1.3, DETECT\_MINAREA = 5 pixels, and a top-hat convolution kernel with a width of 4 pixels.

We forced SE to skip the background-subtraction step, as this was previously removed (Section 3.1). We use MAP\_RMS for the source weighting. As the pipeline-produced ERR images include Poisson noise, they are not appropriate for source detection. We thus convert the weight map associated with the detection image into an effective rms map by taking  $1/\sqrt{\text{WHT}}$  and assign this to the detection image. For the measurement image, we use the pipeline ERR image.

Following previous work (e.g., Finkelstein et al. 2022a), we measure colors in small elliptical apertures, which has been shown to accurately recover the colors of distant galaxies. In SE, these apertures are defined by two parameters: a Kron factor and a minimum radius. We set these two quantities to (1.1, 1.6). These are the same values found by Finkelstein et al. (2022a) via optimization simulations, and we verified via our own simulations (Section 3.3.1) that the S/N in these apertures was significantly better than larger parameters, and that gains in S/N were negligible for smaller values. We estimate an aperture correction to the total flux for these small apertures by performing a second run of SE on the F444W image with the Kron parameters set to the default “MAG\_AUTO” parameters of (2.5, 3.5), deriving an aperture correction as the ratio between the flux in this larger aperture and that in the smaller aperture for each object. The median aperture correction across all four fields was 1.5. This aperture correction was then applied multiplicatively to the fluxes and uncertainties for all filters.

<sup>59</sup> <https://pypher.readthedocs.io>

<sup>60</sup> <https://ceers.github.io/releases.html#sdr3>

### 3.3.1. Residual Aperture Correction

While we use small Kron apertures to derive accurate colors, the aperture correction applied above should yield total fluxes close to the true value. However, several previous studies have noted that the default Kron parameters we use for this aperture correction can miss light in the wings of the PSF (e.g., Bouwens et al. 2015; Finkelstein et al. 2022a), yielding underestimates of the total fluxes at the 5%–20% level.

We estimate these corrections using source-injection simulations, adding 3000 mock sources to our real images in each field. We add sources from  $m = 23$  to 27 mag (to ensure a robust photometric measurement), with a lognormal half-light radius distribution peaking at  $\sim 1.5$  pixels ( $\sim 0.2$  kpc at  $z = 10$ ; compact but modestly resolved, comparable to high-redshift sources; see Section 5.4) and a lognormal Sérsic parameter distribution peaking at 1.2. These mock sources were generated with GALFIT (Peng et al. 2002) and added at random positions to the F277W, F356W, and F444W images. We combined the former two to create a detection image and ran SE in the same way as on our real data to generate an F444W catalog (focusing on this one band, as all images were PSF-matched to F444W). Finally, we match sources in the SE catalog to their input values and compare the ratio of input-to-recovered fluxes. We find a median ratio of 1.08, measured in the range  $25 < m_{F444W} < 26$ . There is a slight trend with magnitude of lower corrections for brighter sources and higher for fainter sources, but only at the 1%–2% level. We thus elect to use a single correction factor of 1.08 to all NIRCcam fluxes and uncertainties.

For the HST fluxes, we elect to derive any residual aperture correction from comparison to the Finkelstein et al. (2022a) photometric catalog, which performed similar simulations to derive total fluxes. Matching sources in each of the six HST bands, we find a typical needed correction factor of  $\sim 1.35$  ( $\pm 0.02$ ). These values are roughly consistent with the combination of the correction derived in Finkelstein et al. (2022a) of 1.20 with the NIRCcam correction derived here of 1.08. We apply this same 1.35 correction to all HST bands, such that the colors among these bands are not changed. We note that in Section 3.6 below, we test for the presence of any remaining photometric offsets in our catalog and find these to be small ( $\lesssim 5\%$ ), indicating that our procedure for deriving total fluxes in all 13 HST + JWST bands is robust, especially for this nascent observatory.

### 3.4. Noise Estimation

While SE does provide an estimate of the noise, it is reliant on the accuracy of the provided error maps. Given the nascent nature of the JWST reduction pipeline, we obtain estimates of our image noise directly from the images themselves. We follow the methods of Finkelstein et al. (2022a), based on previous methodology outlined in Papovich et al. (2016). Our goal is to estimate the noise based on the number of pixels in an aperture. We fit for the noise as a function of aperture size by measuring the fluxes in circular apertures with 30 different diameters, ranging from  $0''.1$  (3.33 pixels) to  $3''$  (100 pixels).

When defining these positions, we restrict aperture placement to pixels with real nonzero values in the ERR image and a zero value in the SE segmentation map within the aperture, avoiding real objects. We also require these apertures to be nonoverlapping to avoid correlating our noise estimation. To

improve statistics for smaller apertures, we placed apertures in two separate iterations: “small” ( $d \leq 1''.5$ ) and “large” ( $d > 1''.5$ ). We were able to place 5000 and 500 nonoverlapping apertures in these two iterations, respectively.

We created a detection image setting the pixels at these positions to unity, with the rest of the image set to zero, and ran SE in two-image mode. We measured fluxes at these positions in all 30 circular apertures with diameters ranging from 1 to 200 pixels. We calculated the  $1\sigma$  noise in each aperture size by measuring the median absolute deviation of the measured flux values (multiplying by 1.48 to convert to a Gaussian-like standard deviation). Finally, we fit a curve to the noise in a given aperture as a function of the pixels in that aperture, using the equation (Gawiser et al. 2006)

$$\sigma_N = \sigma_1 \alpha N^\beta, \quad (1)$$

where  $\sigma_N$  is the noise in an aperture containing  $N$  pixels, and  $\sigma_1$  is the pixel-to-pixel noise measured in each image as the sigma-clipped standard deviation of all nonobject pixels (see Figure 3 in Finkelstein et al. 2022a for an example of this process).

We fit the free parameters  $\alpha$  and  $\beta$  with an IDL implementation of EMCEE (see Finkelstein et al. 2019 for details). We used these functional form fits for each filter to calculate the photometric uncertainties for each object using both the number of pixels in its Kron aperture (area =  $\pi \times A\_IMAGE \times B\_IMAGE \times KRON\_RADIUS^2$ ) and a value for a given circular aperture. These values were scaled by the ratio of the error image value at the central position of a given source to the median error value of the whole map, thereby allowing the noise to be representative of the local noise level.

Finally, to account for variable image noise not captured by the error image value at the central pixel, for each object in our catalog, we also calculate a local noise measurement. This local noise was calculated at  $0''.2$ ,  $0''.3$ ,  $0''.4$ , and  $0''.5$  diameter apertures by fitting a Gaussian to the negative side of the flux distribution in the 200 closest apertures from the above process.

### 3.5. Multiband Catalog

We compose a multiband catalog from the individual-filter catalogs created by SE. As SE cannot parse the world coordinate system in the JWST data model image headers, we use `astropy.wcs.WCS_PIX2WORLD` to derive celestial coordinates from the SE  $x, y$  positions. We apply a photometric zero-point to convert the image from  $\text{MJy sr}^{-1}$  to  $\text{erg s}^{-1} \text{cm}^{-2} \text{Hz}^{-1}$  and apply both aperture corrections derived above to all flux and flux error estimates. We correct for Galactic extinction using an  $E(B - V)$  of 0.006 for the EGS field and a Cardelli et al. (1989) Milky Way attenuation curve.

Both the MAG\_AUTO-derived aperture corrections and simulation-based (and HST catalog-based) residual aperture corrections were applied to all Kron-derived fluxes and uncertainties, maintaining our accurate colors while representing the total fluxes for each source. In our final catalog, we include both these Kron-based fluxes and the fluxes measured in circular apertures with diameters ranging from  $0''.05$  to  $2''.0$ . While the Kron fluxes will be used for most of the analysis, we do use the circular apertures (with a fiducial diameter of  $0''.2$ , or 6.67 pixels) as a measure of detection significance, as the sizes of the Kron apertures can be affected by the proximity to bright sources. These circular apertures are corrected for Galactic

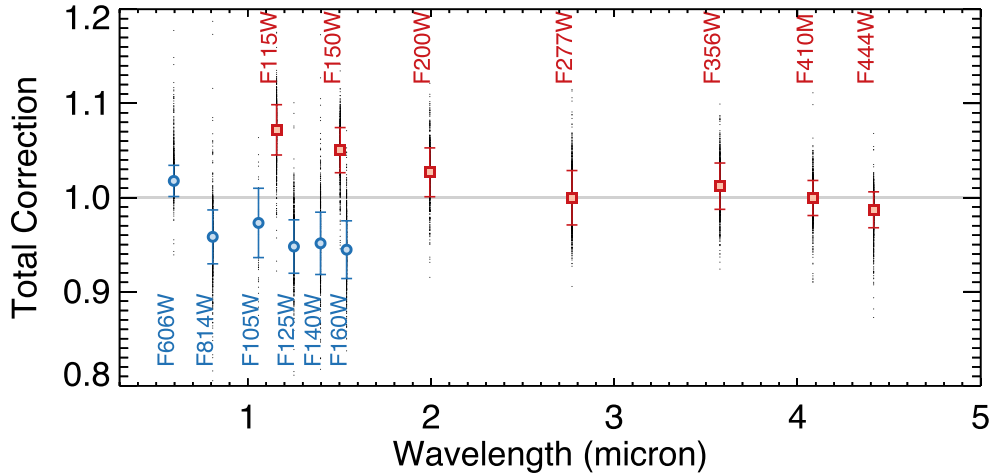


**Figure 2.** Total corrections applied to our catalog to account for residual systematic offsets in our total flux estimations, mismatches between the spectral templates used for photometric redshift fitting, and any remaining photometric calibration corrections (shown as red squares for NIRC*am* and blue circles for HST; small black dots are individual galaxies). These multiplicative offsets were derived by comparing the observed fluxes in each filter to the best-fitting EAZY model templates for  $\sim 900$  sources with robustly known spectroscopic redshifts in our field. The values are tabulated in Table 1.

attenuation but not corrected to total, as we will use them solely for detection significance.

For both the Kron and circular apertures, we calculate the noise per source following the method in Section 3.4, which is dependent on both the aperture area and the effective rms map value at the position of the source. Finally, we flag any sources that had either a zero or NaN in any error column, replacing their flux error with  $10^{12}$  nJy (several orders of magnitude larger than any real source error).

In Table 1, we include an estimate of the limiting  $5\sigma$  magnitude for our catalog. To calculate this, we use the noise functions described above to derive the flux density uncertainty in an aperture of diameter  $0''.2$ . We then measure the enclosed flux at this radius from the stacked PSF. We then divide the flux uncertainty by the enclosed fraction of flux to estimate the total noise for a point source. Finally, we multiply this value by 5 and convert to an AB magnitude. Both the enclosed flux values and the limiting magnitudes are listed in Table 1. While the depths were broadly as expected based on the prelaunch exposure-time calculator, the F115W image (with double the exposure time) was expected to be 0.3 mag deeper. The very low background at that wavelength has led to those images being more read noise-dominated than expected; thus, this image has a depth comparable to the bulk of the NIRC*am* filters. The primary impact is that photometric redshifts will be slightly more uncertain at  $m > 29$  than originally planned.

### 3.6. Photometric Calibration Validation

While the photometric calibration of NIRC*am* has substantially improved over the first few months since science acquisition began, there is still some uncertainty, and many of the reference files still used in the pipeline are preliminary (to be refined during all of Cycle 1; see Boyer et al. 2022 for more details on the NIRC*am* photometric calibration used here). It is thus prudent to check the accuracy of the photometric calibration. The JWST pipeline applies a photometric calibration taking into account the area of each pixel (using a *photom* reference file), resulting in image units of MJy  $\text{sr}^{-1}$ . For the 30 mas scale of our images, the conversion factor from MJy  $\text{sr}^{-1}$  to  $\text{erg s}^{-1} \text{cm}^{-2} \text{Hz}^{-1}$  is  $2.1154 \times 10^{-31}$ .

To check the accuracy of this calibration, we use a sample of objects with published spectroscopic redshifts in this field (compiled by N. Hathi 2022, private communication; including DEEP2, Newman et al. 2013; MOSDEF, Kriek et al. 2015; and 3D-HST, Momcheva et al. 2016, among others). Applying a matching radius of  $0''.5$ , removing duplicates, keeping the two highest-quality redshift flags, and restricting to F160W  $< 24$  mag, we find 988 matches that fall in our CEERS/NIRC*am*-covered area. These objects span  $z = 0-4$ , with a median  $z_{\text{spec}} = 1.1$ .

We generate the expected fluxes of these sources in all 13 photometric bands using the EAZY (Brammer et al. 2008) photometric redshift fitting software. While in Section 4 below, we will use EAZY to measure photometric redshifts, here we run EAZY with the redshift fixed to the spectroscopic redshift value. This thus obtains the best-fitting galaxy template to the observed photometry. Assuming that this template set spans the color range of real galaxies (see Section 4.1), a comparison of the observed fluxes in a given filter to those predicted by EAZY can inform us of any systematic discrepancies in the fluxes in our catalog. We measured the median offset for the subset of these sources with a measured S/N of  $> 5$  and an EAZY goodness of fit ( $\chi^2$ ) of  $< 20$ . This ensures that a well-fit model is found to a set of robust photometric measurements. This typically resulted in  $\sim 850-900$  sources per filter (84 in F105W, which has significantly less coverage), from which we measured a sigma-clipped median and standard deviation.

We tabulate these derived corrections in Table 1 and plot the median values and full dispersion in Figure 2. For NIRC*am*, the LW bands are all consistent with unity, which is a significant improvement over the state of the calibration in late summer 2022. For the SW channels, we find a needed correction on the 3%–7% level. For HST, we find that with the exception of F606W, the remaining bands are  $\sim 3\%-5\%$  too bright. As HST is extremely well calibrated, this implies that the 35% correction we applied based on the comparison to the Finkelstein et al. (2022a) catalog may have been slightly too large (we note that that study did not complete such a zero-point offset analysis). Nonetheless, we applied these corrections. To test their accuracy, we performed another iteration of this analysis after applying these offsets and found that no

significant residual correction was present. We thus apply these corrections, listed in Table 1, to all fluxes and flux errors in our final photometric catalog. We reiterate that while photometric calibration was our motivation for this test, the resulting corrections are a combination of residual differences between our estimated and true total fluxes, differences between the model templates and true galaxies, and true photometric zero-point inaccuracies.

#### 4. Selection of Redshift $>9$ Galaxies

Our analysis method produced a photometric catalog that contains our best estimates of the total fluxes in each of 13 filters spanning 0.6–5.0  $\mu\text{m}$  with robust flux uncertainty values. We also include fluxes measured in a range of circular apertures. In this section, we will use this catalog to select galaxies at  $z > 8.5$ . Below, we will create identifiers for each object inclusive of the CEERS field the object was covered in and the SE number within that field. For example, “Maisie’s Galaxy,” the previously identified  $z \sim 12$  galaxy candidate from Finkelstein et al. (2022b), is referred to here as CEERS2\_5429.

##### 4.1. Photometric Redshift Estimation

We measure photometric redshifts with EAZY for our entire photometric catalog, which contains  $\sim 40,000$  sources across all four fields. EAZY fits nonnegative linear combinations of user-supplied templates to derive probability distribution functions (PDFs) for the redshift based on the quality of fit of the various template combinations to the observed photometry for a given source. The template set we use includes the “tweak\_fps\_QSF\_12\_v3” set of 12 flexible stellar population synthesis (FSPS; Conroy & Gunn 2010) templates recommended by the EAZY documentation.

As shown by Larson et al. (2022b), these recommended templates do not span the blue colors expected for very high redshift galaxies. They developed six additional templates spanning bluer colors by combining stellar population spectra from BPASS (Eldridge & Stanway 2009) with (optional) nebular emission derived with CLOUDY (Ferland et al. 2017). They used models with low metallicities (5% solar), young stellar populations (stellar ages of  $10^6$ ,  $10^{6.5}$ , and  $10^7$  Myr) inclusive of binary stars, and a high ionization parameter ( $\log U = -2$ ). They showed that the inclusion of these templates significantly improved the recovery of photometric redshifts from a mock catalog derived by a semianalytic model (SAM; Yung et al. 2022) due to the better match between galaxy and template colors (see their Figure 4). These templates were also used by Finkelstein et al. (2022b) in their analysis of the  $z \sim 12$  Maisie’s Galaxy, where they found that the inclusion of these bluer templates significantly improved the goodness of fit between the data and the best-fitting model.

We assume a flat prior in luminosity; while bright galaxies will have a redshift distribution significantly tilted toward lower redshift, the bright end of the high-redshift luminosity function is poorly known; thus, we do not wish to bias against the selection of true, bright distant galaxies. We include a systematic error of 5% of the observed flux values and fit to our measured total flux and flux error values. In our fiducial EAZY run, the redshift can span 0–20. We perform an additional “low- $z$ ” run with the maximum redshift set to

$z_{\text{max}} = 7$  such that we can visualize the best-fitting low-redshift solution.

##### 4.2. Sample Selection

Here we describe the selection criteria we use to identify candidate  $z > 8.5$  galaxies. Following our previous work (Finkelstein et al. 2010, 2015, 2022a, 2022b), we utilize a combination of flux detection significance values and quantities derived from the full photometric redshift PDF (denoted  $\mathcal{P}[z]$ ) to select our galaxy sample. As a part of this selection, we make use of the integral of the  $\mathcal{P}(z)$  in  $\Delta z = 1$  bins centered on integer redshift values. Specifically, we denote the unit redshift where the integral in a  $z \pm 0.5$  bin is the maximum compared to all other redshifts as  $\mathcal{S}_z$ . For example, a source with  $\mathcal{S}_z = 10$  would have  $\int_{9.5}^{10.5} \mathcal{P}(z) dz$  greater than the integrated  $\mathcal{P}(z)$  in all other  $\Delta z = 1$  bins.

Our primary selection criteria are as follows.

1. An S/N, as measured in 0".2 diameter apertures in the non-PSF-matched images, of  $> 5.5$  in at least two of the F150W, F200W, F277W, F356W, and F444W bands. We required this to be true with both the global and local noise values. This allows the selection of galaxies across a broad range of redshifts and rest-UV colors. We note that we experimented with requiring a higher-significance detection in just one band, but this significantly increased the spurious source fraction.
2. Error map values  $< 1000$  in all of the F115W, F150W, F200W, and F277W images. This includes only objects with a measurable (though not necessarily significant) flux in the four bluest filters, necessary for selection of galaxies at  $z \sim 9$ –13.
3. An S/N of  $< 3$  in bands blueward of the Ly $\alpha$  break. While studies occasionally use more stringent S/N cuts, we choose this value to account for the fact that any positive flux in all dropout bands is already accounted for by EAZY and that  $> 1\sigma$  random fluctuations can coincide at the positions of real galaxies with non-Gaussian noise, as is present in these images. For this criterion, we include F606W and F814W for all redshifts considered here. We add F115W for  $\mathcal{S}_z = 11$ –12 and F150W for  $\mathcal{S}_z = 13$ –17. These redshift values were chosen to ensure that the Ly $\alpha$  break is fully redward of the  $\Delta z = 1$  range for a given filter.
4.  $\int \mathcal{P}(z > 7) \geq 0.7$ . This requires less than 30% of the integrated  $\mathcal{P}(z)$  to be at  $z < 7$ .
5. Best-fitting photometric redshift  $z_{\text{best}} > 8$  (defined as “za” with EAZY; the redshift corresponding to the highest likelihood) with a goodness-of-fit  $\chi^2 < 60$ .
6.  $\mathcal{S}_z \geq 9$  (selecting a sample of galaxies at  $z \gtrsim 8.5$ ).
7.  $\Delta\chi^2 > 4$ , calculated as the difference between the best-fitting  $\chi^2$  value for the low-redshift restricted model to the fiducial model. By requiring a value greater than 4, we require the low-redshift model to be ruled out at  $\geq 2\sigma$  significance. We note that Harikane et al. (2023) required a more conservative  $\Delta\chi^2 > 9$ , based on results from the CEERS simulated imaging. We explore the impacts of such a cut in Section 7.2.

### 4.3. Sample Vetting

This automated selection resulted in a sample of 64 candidate galaxies with  $z \gtrsim 8.5$ . To explore the impact of potential contamination by spurious (e.g., nonastrophysical) sources, we visually inspected each object in all images to search for obvious diffraction spikes, sources on image edges (as the dithering is different in different filters, the edges do not necessarily line up between different images), and unflagged cosmic rays.

To perform this inspection, three authors (S.F., J.K., and P.A.H.) viewed “bio” plots that showed small  $1''.5$  cutouts of the candidate in all images with two different stretches, a  $5''$  cutout in the F200W and detection images, the fiducial and  $z < 7$  restricted  $\mathcal{P}(z)$ , and the spectral energy distribution (SED) plotted against both fiducial and low- $z$  EAZY models. From this process, we identified 36 spurious sources: six diffraction spikes, 11 unflagged cosmic rays, and 19 sources on image edges. We remove these 36 sources from our galaxy sample, show images of all of them in Figure 20 in Appendix C, and list their positions in Table 6. The cosmic rays were predominantly an issue in the LW image in pointings 3 and 6; these have longer exposure times than pointings 1 and 2, amplifying the impact of cosmic rays. We note that future versions of our images and catalogs should be able to minimize these types of spurious sources by improving the cosmic-ray removal and using the JWST data model “Context map” to identify pixels close to the image edge.

Upon visual inspection, we noticed that a small fraction of the sample (four objects) had Kron apertures that were drawn too large due to the presence of bright, nearby galaxies. To explore the impact of potential light from neighboring galaxies affecting the colors, we performed an additional run of EAZY using the colors measured in  $0''.3$  diameter apertures to more accurately measure the colors of the candidate galaxies. For this run, we used the PSF-matched photometry but did not apply any aperture correction, as the photometric redshift depends only on colors and not luminosity. We found that two sources, CEERS3\_1537 (initial  $z_{\text{phot}} = 10.5$ ) and CEERS6\_7478 (initial  $z_{\text{phot}} = 8.6$ ), had their photometric redshifts shift to lower redshifts with these smaller apertures; these were the same two sources where the Kron aperture was most significantly stretched. We thus remove these two objects from our sample, though we show their SEDs and image stamps in Figure 19 in the Appendix.

The remaining two sources (CEERS1\_3908 and CEERS1\_3910) had no significant change in their photometric redshift when measured with these small apertures. For these two objects, we correct their fluxes by a single factor to account for potential excess brightness from the neighbor. We do this by deriving a flux correction as the ratio between the median total flux for objects with similar  $0''.3$  diameter aperture fluxes as a given source and the actual Kron-based (aperture-corrected) total flux for those comparison sources and dividing this quantity by the same quantity for the sources in question. We apply this correction to all filters such that the colors do not change. For CEERS1\_3908, this correction factor was 0.6; for CEERS1\_3910, it was close to unity, so we applied no correction.

## 5. An Early Redshift $>9$ JWST Galaxy Sample

Our final sample consists of 26 galaxies. We divide them into redshift bins for analysis. The high redshifts now accessible with JWST coupled with the broad filter transmission functions make it harder to place galaxies in often-used  $\Delta z = 1$  redshift bins, and such bins span progressively smaller epochs of cosmic time (for example, a  $\Delta z = 1$  bin centered at  $z = 12$  would cover the Ly $\alpha$  break over only  $\sim 40$  Myr of cosmic time, compared to 200 Myr for one centered at  $z = 6$ ). We thus split our sample into three redshift bins: a  $z \sim 9$  sample from  $z = 8.5$  to 10, a  $z \sim 11$  sample from  $z = 10$  to 12, and a  $z > 12$  sample from  $z = 12$  to 17. We place candidate galaxies in the sample bin based on where their integrated  $\mathcal{P}(z)$  across the bin is the largest. These three bins cover roughly similar ranges of cosmic time (116, 105, and 122 Myr, respectively). We show the distribution of the photometric redshifts and apparent magnitudes of our sample in Figure 3, and we tabulate the sample in Table 2. We show cutout images of all candidates in Figures 5, 6, 16, and 17 and SEDs in Figures 5, 7, and 18. We also present a rest-UV color montage of our sample in descending redshift order in Figure 4.

As a check on our fiducial EAZY photometric redshifts, we also measured photometric redshifts with Cigale (Burgarella et al. 2005). We find excellent agreement, with a median difference of 0.2 (with EAZY preferring the slightly higher redshifts). Only the source CEERS1\_4143 has a difference in best-fitting redshift of  $>2$ , as Cigale prefers  $z = 5.4$  for this source, whereas EAZY finds  $z = 9.0$ , though this source lies right at the boundary of our  $\Delta\chi^2$  selection criterion. Finally, we inspect the spatial distribution of our full sample of galaxies across the full CEERS field and do not visually see any evidence of strong clustering (which would not be expected with such a small sample covering a broad redshift range).

### 5.1. The $z > 12$ Sample

This highest-redshift sample contains two galaxies, CEERS2\_2159 and CEERS1\_1730, with 68% confidence ranges on their photometric redshifts of 16.0–16.6 and 12.3–14.2 and F277W magnitudes of 26.5 and 27.7, respectively. We will compare our sample in detail to those previously presented in the literature in Section 6 below, but we note here that CEERS2\_2159 was first presented as a robust ultrahigh-redshift candidate in D23, with some caveats discussed in Zavala et al. (2023; a marginal  $2.6\sigma$  dust emission detection) and Naidu et al. (2022a; environmental evidence). CEERS1\_1730 is presented here for the first time.

The cutout images for these two objects are shown in the top panel of Figure 5. It is apparent that there is no significant flux at the positions of both candidates in the stacked ACS F606W + F814W images or the F115W image. For CEERS2\_2159, no flux is also seen in F150W, and the F200W flux is noticeably fainter than in F277W, consistent with its photometric redshift of  $z \sim 16$ –16.6 (where the Ly $\alpha$  break would be in the red half of the F200W bandpass). For CEERS1\_1730, faint flux is seen in F150W. However, this is measured at just  $1\sigma$  significance in the Kron aperture. This leads to a fairly broad  $\mathcal{P}(z)$ , spanning  $z \sim 12$ –14. If this flux is real, then  $z \sim 12$  is more likely. If it is not significant, then  $z \sim 14$  is possible. The SEDs, shown in the bottom panel of Figure 5, show the strong observed Ly $\alpha$  break in both objects, with fairly blue UV spectral slopes redward of the break. For both objects, the high-redshift model is a

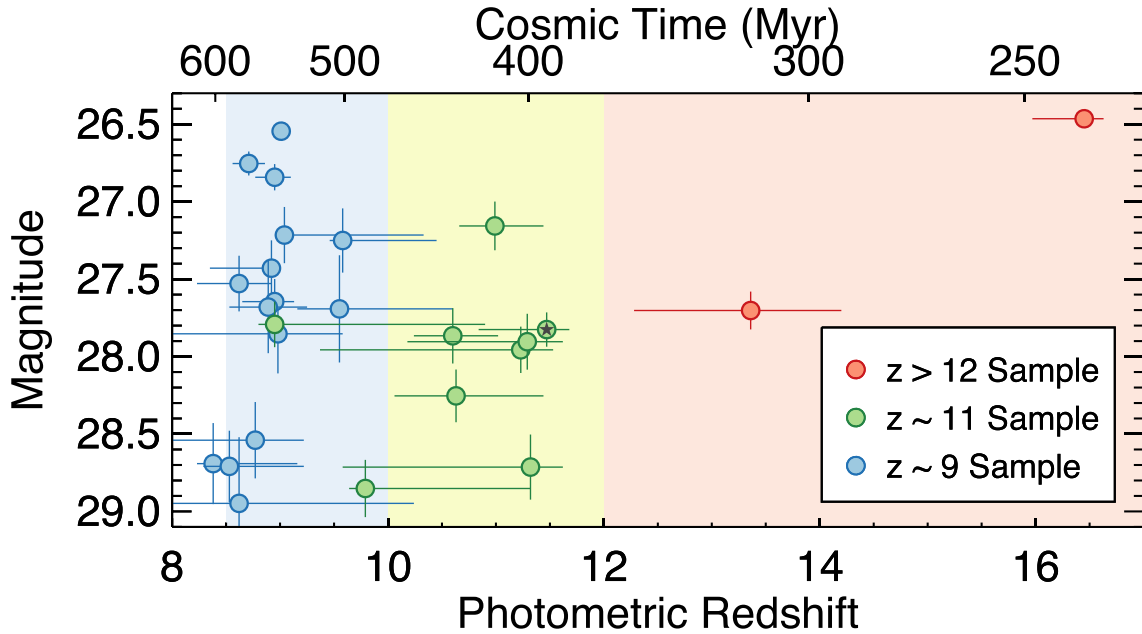


**Figure 3.** Distribution of the best-fitting (minimized  $\chi^2$ ) photometric redshift vs. apparent magnitude. Each object is color-coded by its redshift sample (with the background shading denoting the redshift range where the  $\mathcal{P}(z)$  was integrated to determine the sample placement; the green circle far into the blue region [CEERS6\_7641] has a double-peaked  $\mathcal{P}(z)$ ). The magnitude plotted is F150W for  $z \sim 9$ , F200W for  $z \sim 11$ , and F277W for  $z > 12$  galaxies. The small black star denotes Maisie’s Galaxy (Finkelstein et al. 2022b), known here as CEERS2\_5429. The top axis shows the cosmic time (the time since the Big Bang) for our adopted cosmology.

significantly better fit to the photometry than the best-fitting low-redshift model, though for CEERS1\_1730,  $\Delta\chi^2$  is only 4.4; this low-redshift solution is visible as a small peak in the fiducial  $\mathcal{P}(z)$ . CEERS2\_2159 shows no significant lower-redshift peak in its  $\mathcal{P}(z)$  due to its brighter magnitude, leading to more robust constraints on the full shape of the SED.

### 5.2. The $z \sim 11$ Sample

The  $z \sim 11$  sample contains nine galaxies. As shown by their cutout images in Figure 6, all show no significant flux in the ACS stack and F115W images, consistent with  $z > 9.5$ . Many exhibit a red F150W–F200W color, suggesting that the Ly $\alpha$  break is in F150W. The SEDs and  $\mathcal{P}(z)$ s for all nine are shown in Figure 7. First looking at the  $\mathcal{P}(z)$ s in the upper left of each panel, the amplitude of the detected Ly $\alpha$  break is strong enough to either eliminate or leave a very small low-redshift solution. As shown in Table 2, the integrated  $\mathcal{P}(z > 7)$  is  $\geq 0.98$  for eight out of nine of these sources, with the remaining source (CEERS1\_7227) having a value of 0.85, significantly greater than our sample limit of 0.7 (this object also just barely satisfies our  $\Delta\chi^2$  criterion, as only the F200W flux is discrepant with the best-fitting lower-redshift model, and it has a  $2.2\sigma$  significance detection in F115W, which could indicate a redshift closer to  $z \sim 9$ ).

CEERS6\_7641 shows a double-peaked high-redshift  $\mathcal{P}(z)$  with peaks at  $z \sim 9$  and 11. As its integrated  $\mathcal{P}(z)$  at  $z = 10$ –12 is larger than at  $z = 8.5$ –10, this object was placed in the  $z \sim 11$  sample (this is the green  $z \sim 11$  symbol in Figure 3 that is in the  $z \sim 9$  sample region), though clearly, it has a near-equal probability of being at a slightly lower redshift. Finally, we note that, similar to the  $z > 12$  galaxies, the UV spectral slopes for these nine sources all appear fairly blue. Though a detailed analysis of this quantity is beyond the scope of this paper, it is clear that these objects all appear fairly low in dust attenuation.

We acknowledge that Ly $\alpha$  break selection can be biased against red sources (e.g., Dunlop et al. 2012); thus, a full quantitative analysis of the colors of these galaxies is reserved for future work.

### 5.3. The $z \sim 9$ Sample

The remaining 15 candidate high-redshift galaxies fall into our  $z \sim 9$  sample. We show the cutout images in Figures 16 and 17 in the Appendix. At  $z < 9.5$ , the Ly $\alpha$  break is in the F115W band; thus, we expect to see signal in that image for all but the highest-redshift sources in this subsample, though the F115W flux should be fainter than the F150W flux, which is apparent in the images. Likewise, we see no significant flux in the ACS filters, as expected. Examining their SEDs and  $\mathcal{P}(z)$ s in Figure 18 in the Appendix, we see that nearly all show a tight high-redshift peak with very little probability of being at  $z < 7$ . Similar to the  $z \sim 11$  sample, the lowest integrated  $\mathcal{P}(z > 7)$  is 0.84, with 13 out of 15 galaxies having integrated  $\mathcal{P}(z > 7) > .9$  and eight out of 15 having integrated  $\mathcal{P}(z > 7) \geq 0.99$ .

The object with the most complex  $\mathcal{P}(z)$  constraints is CEERS2\_2274, which shows small peaks at  $z \sim 2$  and 6, a dominant peak at  $z \sim 9$ , and a modest peak at  $z \sim 10.5$ , with this uncertainty due to the lower S/N on this object’s faint fluxes. While the majority of these  $z \sim 9$  galaxies show blue rest-UV spectral slopes, the lower redshift means that the reddest filters probe the 4000 Å breaks, and it is clear that some objects have redder colors in these reddest bands. This may be due to significant stellar mass in (somewhat) older stellar populations (e.g., Labbe et al. 2022), though it could also be due to the presence of very strong rest-frame optical nebular emission lines, which early JWST results indicate are ubiquitous in high-redshift star-forming galaxies (Endsley et al. 2022; C. Papovich et al. 2022, in preparation).

**Table 2**  
Summary of  $z > 9$  Candidate Galaxies

ID	R.A. (J2000)	Decl. (J2000)	$m_{F277W}$ (mag)	$\int_7^{20} \mathcal{P}(z)$	Sample $S_z$	Photometric Redshift	$M_{1500}$ (mag)	$R_h$ (pixels)	$\Delta\chi^2$
CEERS2_2159	214.914548	52.943023	26.5	1.00	>12	16.45 <sup>+0.18</sup> <sub>-0.48</sub>	-21.7 <sup>+0.1</sup> <sub>-0.1</sub>	4.4 ± 6.0	4.4
CEERS1_1730	215.010022	53.013641	27.7	0.97	>12	13.36 <sup>+0.84</sup> <sub>-1.08</sub>	-20.4 <sup>+0.2</sup> <sub>-0.2</sub>	5.3 ± 1.0	15.0
CEERS2_588	214.906633	52.945504	26.9	0.98	11	10.99 <sup>+0.45</sup> <sub>-0.33</sub>	-20.6 <sup>+0.2</sup> <sub>-0.2</sub>	4.0 <sup>a</sup>	7.4
CEERS1_8817	215.043999	52.994302	28.1	1.00	11	10.60 <sup>+0.42</sup> <sub>-0.36</sub>	-19.7 <sup>+0.2</sup> <sub>-0.2</sub>	2.4 ± 0.7	12.1
CEERS2_7929	214.922783	52.911528	28.1	0.99	11	11.29 <sup>+0.33</sup> <sub>-1.11</sub>	-19.8 <sup>+0.4</sup> <sub>-0.1</sub>	4.1 ± 1.0	9.1
CEERS6_7641	214.897232	52.843854	28.1	0.99	11	8.95 <sup>+1.95</sup> <sub>-0.15</sub>	-19.3 <sup>+0.1</sup> <sub>-0.2</sub>	2.0 ± 0.6	8.8
CEERS2_5429 <sup>b</sup>	214.943148	52.942442	28.3	1.00	11	11.47 <sup>+0.21</sup> <sub>-0.63</sub>	-19.9 <sup>+0.2</sup> <sub>-0.3</sub>	4.6 ± 1.2	25.8
CEERS1_7227	215.037504	52.999394	28.3	0.85	11	11.23 <sup>+0.30</sup> <sub>-1.86</sub>	-19.7 <sup>+0.3</sup> <sub>-0.1</sub>	6.4 ± 2.6	4.0
CEERS6_7603	214.901252	52.846997	28.9	0.98	11	11.32 <sup>+0.30</sup> <sub>-1.74</sub>	-18.8 <sup>+0.4</sup> <sub>-0.2</sub>	2.1 ± 0.8	7.1
CEERS6_4407	214.869661	52.843646	29.0	0.99	11	10.63 <sup>+0.81</sup> <sub>-0.57</sub>	-19.1 <sup>+0.2</sup> <sub>-0.3</sub>	4.2 ± 1.2	9.3
CEERS6_8056	214.850129	52.808052	29.1	0.99	11	9.79 <sup>+1.53</sup> <sub>-0.15</sub>	-18.4 <sup>+0.1</sup> <sub>-0.4</sub>	2.0 ± 0.7	7.2
CEERS2_2402	214.844766	52.892104	26.7	1.00	9	8.71 <sup>+0.15</sup> <sub>-0.15</sub>	-20.5 <sup>+0.1</sup> <sub>-0.0</sub>	4.9 ± 0.7	63.9
CEERS1_6059	215.011706	52.988303	27.0	1.00	9	9.01 <sup>+0.06</sup> <sub>-0.06</sub>	-20.6 <sup>+0.0</sup> <sub>-0.1</sub>	2.6 ± 0.4	48.0
CEERS1_1875	214.951936	52.971742	27.1	0.92	9	8.92 <sup>+0.06</sup> <sub>-0.57</sub>	-19.9 <sup>+0.3</sup> <sub>-0.1</sub>	8.4 ± 1.3	5.4
CEERS1_3858	214.994402	52.989379	27.2	0.99	9	8.95 <sup>+0.15</sup> <sub>-0.18</sub>	-20.4 <sup>+0.1</sup> <sub>-0.1</sub>	2.1 ± 0.5	7.6
CEERS2_7534	214.876144	52.880826	27.4	1.00	9	8.95 <sup>+0.18</sup> <sub>-0.30</sub>	-19.5 <sup>+0.2</sup> <sub>-0.1</sub>	1.4 ± 0.3	39.6
CEERS1_3908	215.005189	52.996580	27.3	0.96	9	9.04 <sup>+1.29</sup> <sub>-0.06</sub>	-20.1 <sup>+0.1</sup> <sub>-0.3</sub>	10.0 <sup>c</sup>	5.3
CEERS6_4012	214.888127	52.858987	27.6	0.92	9	8.89 <sup>+0.36</sup> <sub>-0.36</sub>	-20.0 <sup>+0.2</sup> <sub>-0.2</sub>	5.5 ± 2.0	4.8
CEERS2_2324	214.861602	52.904603	27.6	1.00	9	9.58 <sup>+0.87</sup> <sub>-0.12</sub>	-20.1 <sup>+0.2</sup> <sub>-0.2</sub>	2.0 ± 0.8	10.7
CEERS1_3910	215.005365	52.996697	28.0	0.96	9	9.55 <sup>+1.05</sup> <sub>-0.39</sub>	-19.5 <sup>+0.5</sup> <sub>-0.2</sub>	8.6 ± 1.4	5.7
CEERS1_5534	214.950078	52.949267	27.9	1.00	9	8.62 <sup>+0.30</sup> <sub>-0.39</sub>	-19.5 <sup>+0.2</sup> <sub>-0.2</sub>	3.6 ± 0.7	12.6
CEERS1_4143	214.966717	52.968286	28.1	0.84	9	8.98 <sup>+0.60</sup> <sub>-1.23</sub>	-19.5 <sup>+0.3</sup> <sub>-0.2</sub>	4.8 ± 1.5	4.0
CEERS3_1748	214.830685	52.887771	28.5	0.93	9	8.77 <sup>+0.45</sup> <sub>-1.08</sub>	-18.3 <sup>+1.0</sup> <sub>-0.2</sub>	1.8 ± 0.7	4.2
CEERS2_1298	214.902236	52.939370	28.6	1.00	9	8.53 <sup>+0.69</sup> <sub>-0.24</sub>	-18.4 <sup>+0.2</sup> <sub>-0.4</sub>	2.2 ± 0.8	12.7
CEERS2_2274	214.846173	52.894001	29.1	0.85	9	8.62 <sup>+1.62</sup> <sub>-1.41</sub>	-18.6 <sup>+0.3</sup> <sub>-0.4</sub>	1.8 ± 0.8	4.2
CEERS2_1075	214.907627	52.944611	29.1	1.00	9	8.38 <sup>+0.78</sup> <sub>-0.15</sub>	-18.4 <sup>+0.2</sup> <sub>-0.3</sub>	1.6 ± 0.7	12.7

**Notes.** The horizontal lines divide our three redshift samples (given by the sixth column). The photometric redshift is “za” from EAZY, which is the redshift where the  $\chi^2$  is minimized. The  $\Delta\chi^2$  in the final column compares the best-fitting low-redshift ( $0.5 < z < 7$ ) model to the best-fitting high-redshift model; a value of  $\geq 4$  was required for selection.

<sup>a</sup> GALFIT did not converge for these two sources, so we list their SE half-light radii.

<sup>b</sup> Previously published as Maisie’s Galaxy by Finkelstein et al. (2022b). The half-light radii are listed in pixels; our pixel scale is 30 mas.

Finally, we discuss the interesting pair of objects CEERS1\_3908 and CEERS1\_3910. As discussed in Section 4.3, the presence of a bright neighbor skewed their Kron apertures, but even after correcting for this, they appear as robust  $z \sim 9$  candidates. In inspecting their cutout images, it is apparent that these two candidate galaxies are very close together, with each consisting of a small knot of emission with centroids  $0''.6$  ( $\sim 2.5$  kpc) apart. It is possible that these are two star-forming regions of the same host galaxy. This hypothesis could be supported by the apparent very faint emission between the two clumps. Deeper imaging could resolve this, though as they are resolved in our catalog, we do not merge them here.

As one additional check, we explored the impact of our photometric correction factors (Section 3.6), which we had applied to our catalog. We reran EAZY on our final sample of 26 high-redshift galaxy candidates removing this factor. We find that this makes effectively no change in the high-redshift solution, with the best-fitting redshifts unchanged to more than the 1%–2% level and all candidates continuing to satisfy our  $\mathcal{P}(z)$  selection criteria. We did notice a slight change in the best-fitting low-redshift model, leading to the median value of  $\Delta\chi^2$  being reduced by 5%. This impacts sources that were close to our  $\Delta\chi^2$  threshold, with CEERS1\_1730 ( $\Delta\chi^2 = 4.4 \rightarrow$

3.5), CEERS1\_4143 ( $\Delta\chi^2 = 4.0 \rightarrow 3.7$ ), and CEERS1\_7227 ( $\Delta\chi^2 = 4.0 \rightarrow 3.7$ ) falling below our threshold of  $\Delta\chi^2 > 4$ . While these sources remain in the sample following our fiducial selection, their presence near this threshold leaves their inclusion more sensitive to these small correction factors.

#### 5.4. Galaxy Sizes

We derive the sizes of all 26 galaxies in the sample by performing parametric fits on the F200W NIRCcam images using GALFIT<sup>61</sup> (Peng et al. 2002, 2010). GALFIT finds the optimum Sérsic fit to a galaxy’s light profile using a least-squares fitting algorithm. As input, we use a  $100 \times 100$  pixel cutout of the F200W image for each source, the corresponding error array (the ERR extension) as the input sigma image, and the empirically derived PSFs. We use the source location, magnitude, size, position angle, and axis ratios from the SE catalog as initial guesses. We allow the Sérsic index to vary between 0.01 and 8, the magnitude of the galaxy between zero and 45, the half-light radius ( $r_h$ ) between 0.3 and 100 pixels, and the axis ratio between 0.0001 and 1. We also allow GALFIT to oversample the PSF by a factor of 9. We then visually

<sup>61</sup> <https://users.obs.carnegiescience.edu/peng/work/galfit/galfit.html>

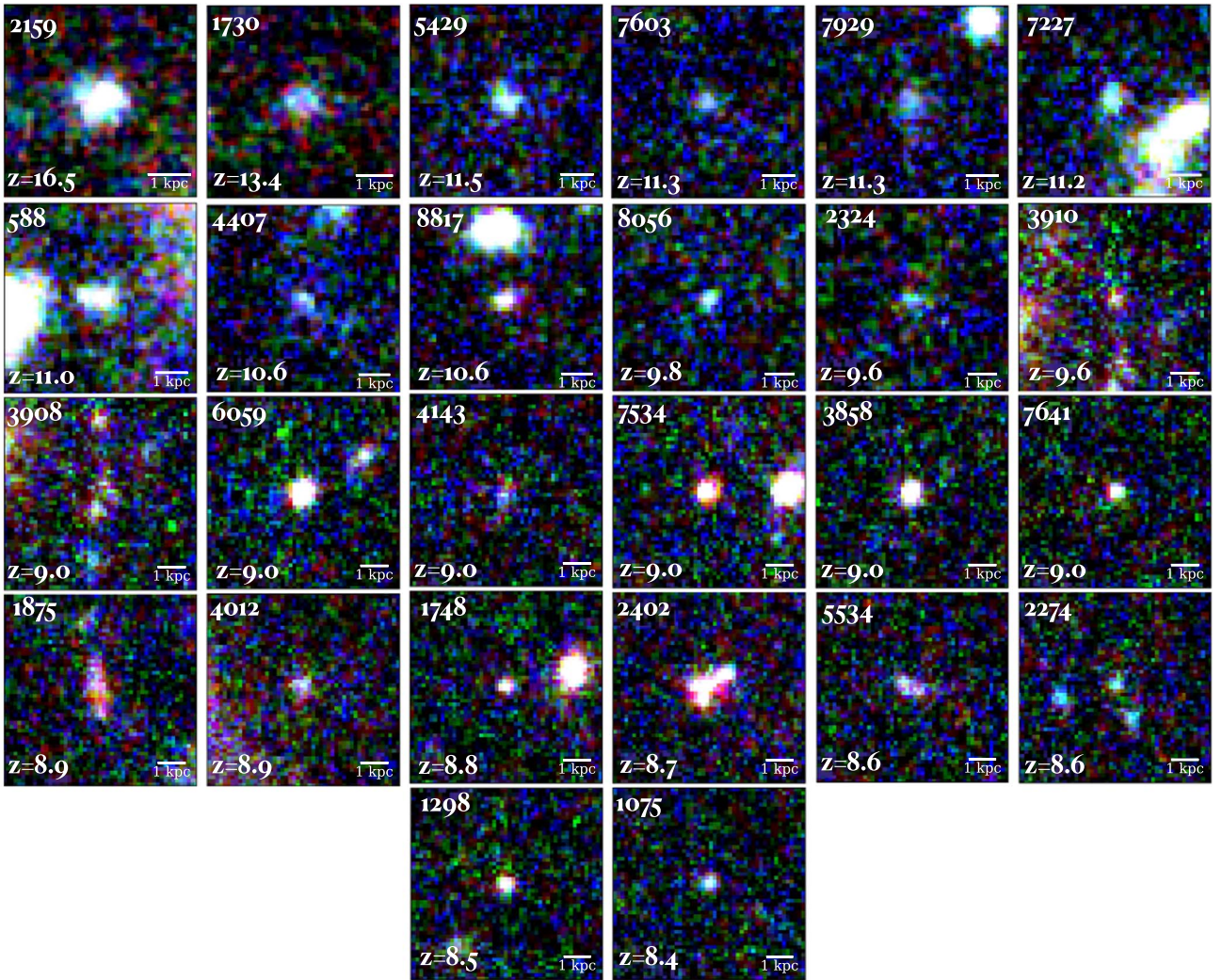


**Figure 4.** Montage of images for the galaxy candidates identified here. For each galaxy, the image shows as blue–green–red the three NIRCcam bandpasses closest to the Ly $\alpha$  break, which includes F150W, F200W, and F277W for galaxies at  $z = 9$ ; F200W, F277W, and F356W for galaxies in the  $z = 10$ –12 samples; and F277W, F356W, and F444W for galaxies in the  $z \geq 12$  samples. In each case, the images are  $1''.5 \times 1''.5$ . The inset scale bar shows 1 (physical) kpc. We list the numerical IDs and best-fitting photometric redshift values (the redshift uncertainties are listed in Table 2).

inspected the best-fit model and image residual for each source to ensure that the fits were reasonable and that minimal flux remained in the residual. We also performed a fit on the PSF image itself in order to determine the smallest resolvable size. This value is  $1.18 \pm 0.01$  pixels. Two sources (CEERS1\_3908, a member of the pair discussed above, and CEERS2\_588) failed to converge on a fit.

In Figure 8, we show these measured sizes, highlighting that the majority of the sample is significantly spatially resolved. The measured  $r_h$  values range from 0.41 to 8.59 pixels, with a median value of 3.6 pixels ( $0''.11$  or 0.46 kpc). These sizes are consistent with the rest-UV sizes found in the GLASS survey by Yang et al. (2022), who found a median half-light radius of  $0.45 \pm 0.13$  kpc for galaxies at  $7 < z < 15$ .

### 5.5. Stellar Contamination Screening

It is important to analyze whether any objects in our sample could potentially be low-mass stars or brown dwarfs, as they can have similar colors as high-redshift galaxies when observed in broadband filters (e.g., Yan et al. 2003; Ryan et al. 2005;

Caballero et al. 2008; Wilkins et al. 2014). We first analyze the GALFIT-produced half-light radii of our candidates, as any resolved objects cannot be stellar in origin. Figure 8 shows the GALFIT-measured radii for the 24 out of 26 of our candidate high-redshift galaxies where GALFIT converged (showing the SE values for the remaining two). We find that the majority of the sample is obviously resolved, with only five of the faintest sources having sizes within the  $1\sigma$  error bars that allow for a point source.

For these five unresolved sources, we then follow the methodology of Finkelstein et al. (2022a, 2022b) to explore whether the colors of any of the few unresolved galaxy candidates could be consistent with stars. We derive a grid of models for the colors of low-mass stars and brown dwarfs (spectral types of M4–T8) in the NIRCcam filters by integrating the IRTF SpEX brown dwarf templates (Burgasser 2014). As these spectra end at  $2.5 \mu\text{m}$ , we use the tabulated 2MASS photometry to link each SpEX model with Spitzer/IRAC photometry from Patten et al. (2006). Following Finkelstein et al. (2022b), we assume we can map IRAC  $3.6 \mu\text{m}$  onto F356W and  $4.5 \mu\text{m}$  onto F444W, though future spectroscopic

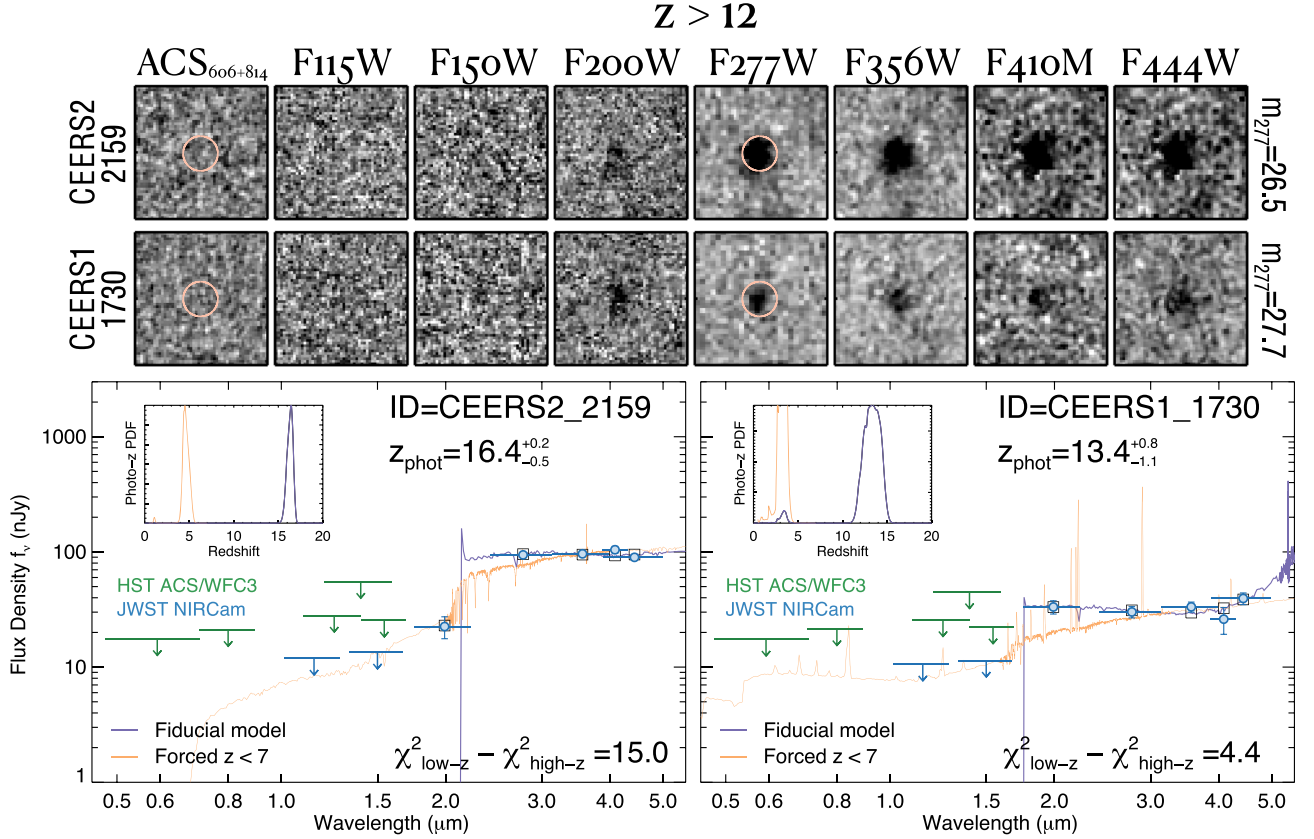


**Figure 5.** Top: stamp images,  $1''/5$  on a side, of the two galaxies that are best fit with  $z > 12$  (shown from the non-PSF-matched images). The red circle denotes a  $0''.4$  diameter region around the source (which we show in only two bands for clarity). CEERS1\_1730 has a best-fit photo- $z$  of 13.4, albeit with a wide 68% confidence range of 12.3–14.2. CEERS2\_2159 is best fit by  $z = 16.5$  (16.0–16.6) and was first identified by D23. The bottom panels show the best-fitting EAZY models (both overall and constrained to  $z < 7$ ), the model bandpass fluxes (open squares), and the observed photometry (circles; upper limits are  $2\sigma$ ). The inset panels show the  $\mathcal{P}(z)$  distributions. Both sources exhibit well-constrained Ly $\alpha$  breaks, implying that the redshifts are  $z > 11$ . CEERS1\_1730 does show a small low-redshift solution, and its primary  $\mathcal{P}(z)$  peak extends to  $z \sim 10.5$ .

observations of brown dwarfs with JWST at  $\lambda \gtrsim 2.5 \mu\text{m}$  will improve this methodology. To explore which model is preferred, we use the Bayesian information criterion (BIC), which includes the goodness of fit ( $\chi^2$ ), the number of photometric constraints (five for stars and 12 for galaxies due to the use of HST for the latter), and the number of free parameters (one for stars and 19 for galaxies, with 18 templates fit simultaneously, plus the redshift). We find that two of these five sources have BIC values that indicate a preference for the best-fitting stellar model.

Although these two objects (CEERS2\_2274 and CEERS2\_1075) are formally unresolved and have optical/near-IR colors consistent with brown dwarfs (Patten et al. 2006), we nevertheless doubt this interpretation, as they are very faint ( $m_{\text{F277W}} = 29.1$  mag). The colors imply a very late spectral type of  $\gtrsim \text{T5}$ , which corresponds to an absolute magnitude of  $K = 16.1$  AB mag (Patten et al. 2006). Such a brown dwarf would therefore be at a heliocentric distance of 3.6 kpc, or 3.1 kpc above the Galactic plane, which would place this object approximately nine scale heights out of the thin disk (e.g., Ryan et al. 2011; Holwerda et al. 2014). These objects are therefore highly unlikely to be part of the Population I thin disk stars but could be members of the thick disk or Galactic halo (Ryan & Reid 2016). At present, there are very few constraints on the density of brown dwarfs in these more distant Galactic components at these extremely low

effective temperatures, but based on more massive main-sequence stars, these are expected to have many orders of magnitude fewer stars than the thin disk (e.g., Jurić et al. 2008). A rigorous Bayesian model of the halo brown dwarfs would provide the strongest statistical evidence and prediction for or against this source, but this is beyond the scope of the present work. We also note that CEERS2\_2274 appears to have a very nearby neighbor with a similar SED, which could indicate that it is a merging system at high redshift. We note that both sources are below the brightness limit ( $m < 28.5$ ) we apply when analyzing our sample in Section 7, so their inclusion (or exclusion) does not affect any of our conclusions.

### 5.6. Examining Ancillary Multiwavelength Observations

We have examined the positions of our 26 candidate  $z \gtrsim 9$  galaxies at both shorter and longer wavelengths and find no significant detections, increasing confidence in the very high redshift interpretation. While the depth of these data is not necessarily sufficient to completely rule out low-redshift solutions, these nondetections do increase our confidence in the fidelity of our sample. First, we searched for X-ray emission coincident with our candidate positions using Chandra imaging from the AEGIS-XD survey (Nandra et al. 2015), which has a flux limit of  $1.5 \times 10^{-16} \text{ erg cm}^{-2} \text{ s}^{-1}$  in the 0.5–10 keV band. There was no emission detected, with a Poisson false

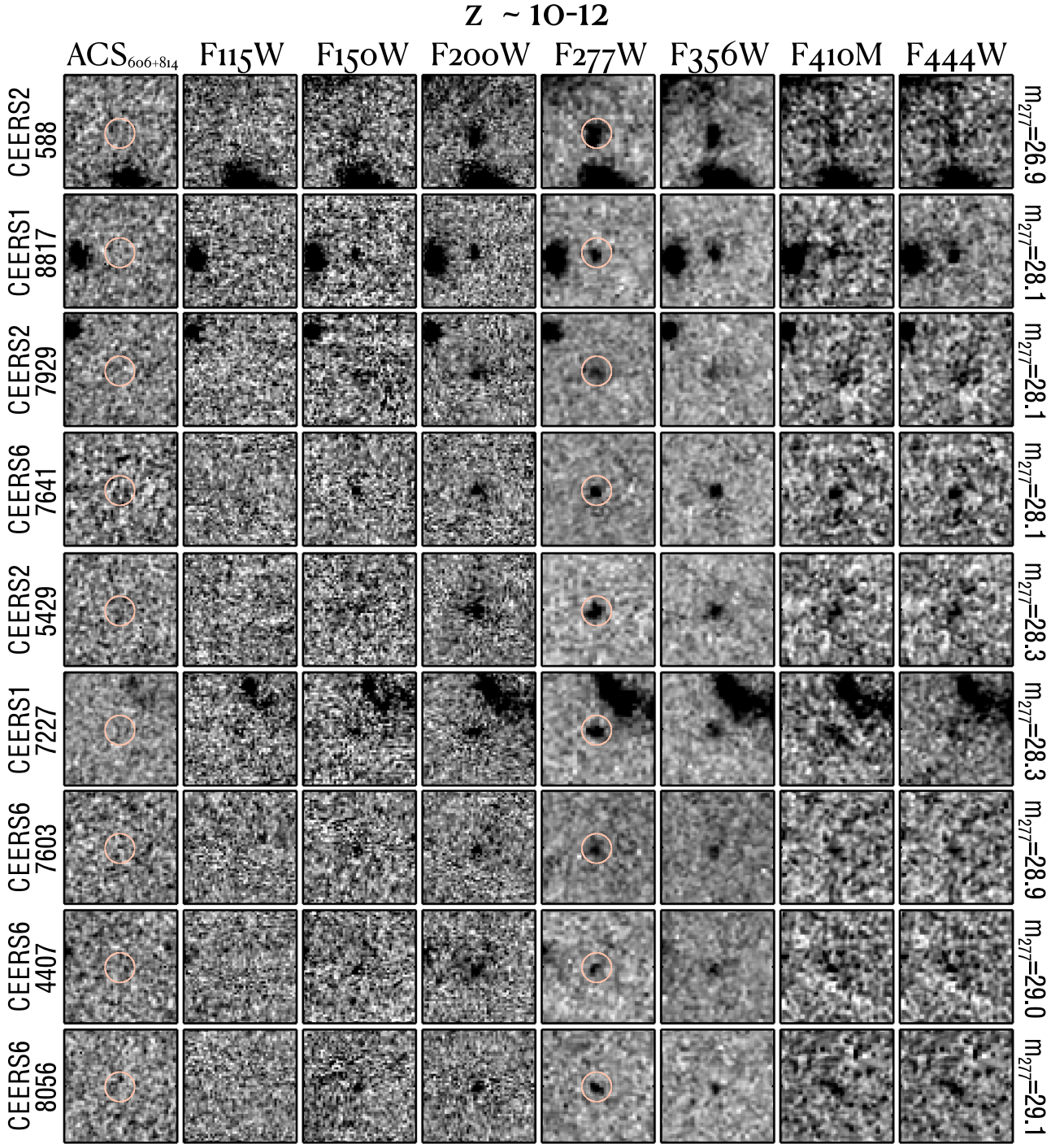
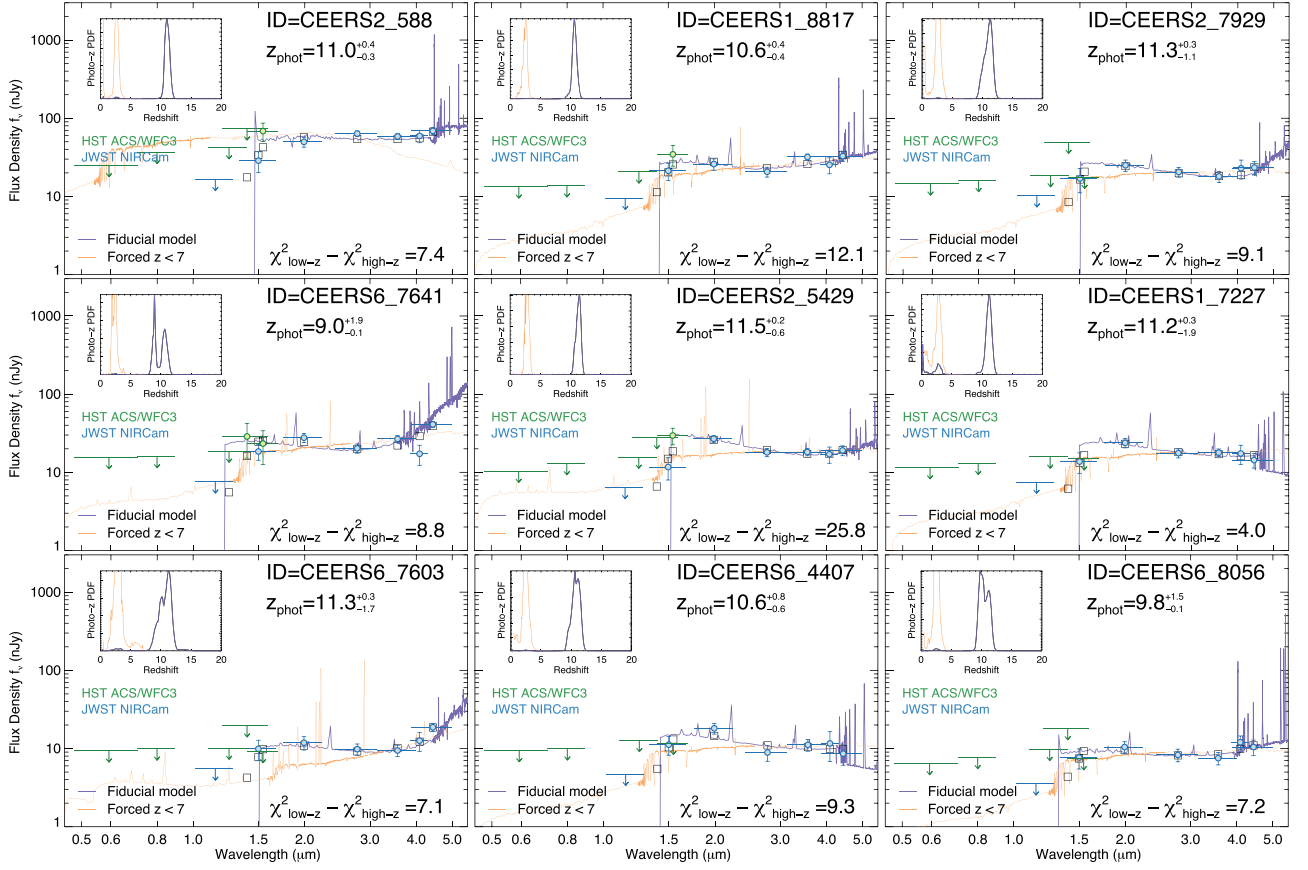


Figure 6. Similar to Figure 5 for the nine galaxies in the  $z \sim 11$  sample.

probability of less than  $4 \times 10^{-6}$  in the soft (0.5–2 keV), hard (2–7 keV), full (0.5–7 keV), and ultrahard (4–7 keV) energy bands.

We then investigated possible far-infrared emission at the position of our high-redshift galaxy candidates using the superdeblending catalog technique from Jin et al. (2018) and Liu et al. (2018), which was adapted for the EGS field. To summarize, this multiwavelength fitting technique is meant to optimize the number of priors fitted at each band to extract the deepest possible information. For this multiwavelength

fitting, we use data from Spitzer (24  $\mu\text{m}$  from FIDEL; Dickinson & FIDEL Team 2007), Herschel 100  $\mu\text{m}$  and 160  $\mu\text{m}$  from PEP (Lutz et al. 2011) and 250  $\mu\text{m}$ , 350  $\mu\text{m}$ , 500  $\mu\text{m}$  from HerMES (Oliver et al. 2012), JCMT/SCUBA-2, including 850  $\mu\text{m}$  from S2CLS (Geach et al. 2017) and 450  $\mu\text{m}$  and 850  $\mu\text{m}$  from Zavala et al. (2017) and AzTEC 1.1 mm from Aretxaga (2015). The key is to obtain an adaptive balance as a function of wavelength/data set between the number of priors fitted, the quality of the fit, and the achievable deblending given the PSF sizes. We start



**Figure 7.** The SEDs and  $\mathcal{P}(z)$ s for the  $z \sim 10$ –12 sample, with lines and symbols the same as in Figure 5.

with the deepest images and fit each band from deeper to shallower images.

In general, the high-redshift galaxy candidates are not already contained in our prior lists, with the exception of two sources, for which all measurements are already contained in the forthcoming catalog (A. Le Bail et al. 2022, in preparation). For the other candidates, we consider them one at a time and add a specific prior at its position that we fit together with the rest of the priors that are relevant for each band. Extensive Monte Carlo simulations ensure that the uncertainties associated with the flux measurements are “quasi-Gaussians” (see Jin et al. 2018; Liu et al. 2018; A. Le Bail et al. 2022, in preparation). None of the candidates are significantly detected at any band between  $24 \mu\text{m}$  and  $1.1 \text{ mm}$ . We note that for one galaxy, CEERS1\_1730, this method implies an  $\sim 3\sigma$  detection at  $500 \mu\text{m}$ . However, inspecting the images, it is clear at  $160$ ,  $250$ , and  $350 \mu\text{m}$ , there is significant emission from a bright neighbor to the south, which overlaps our source’s position at  $500 \mu\text{m}$  due to the worsening PSF. We conclude that it is highly unlikely that this emission is associated with our candidate.

We also note that our object CEERS2\_2159, first published as ID = 93316 by D23, has a formal  $2.6\sigma$  detection in the SCUBA-2  $850 \mu\text{m}$  data, as noted by Zavala et al. (2023). However, that marginal  $850 \mu\text{m}$  detection could plausibly be associated with other nearby  $z \sim 5$  galaxies within the beam, as discussed in Zavala et al. (2023); higher-resolution millimeter interferometry is being carried out on this system to gain further insight (S. Fujimoto et al. 2022, in preparation).

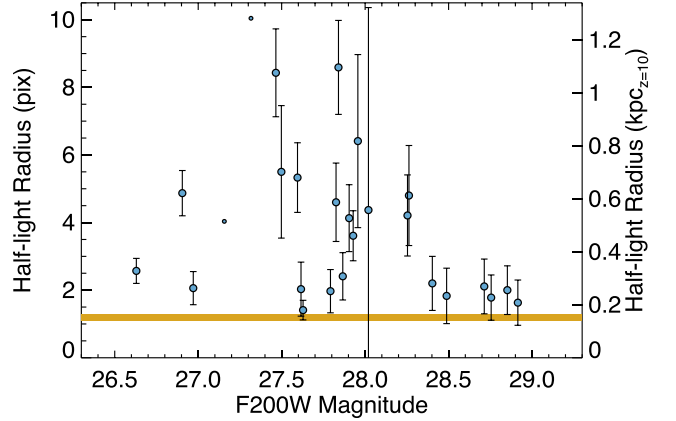


**Figure 8.** The F200W half-light radii of our high-redshift galaxy candidates, measured with GALFIT. The shaded region denotes the half-light radius for the F200W PSF of  $1.18 \pm 0.01$  pixels (our pixel scale is  $30 \text{ mas}$ ). While the galaxies are compact, all but the faintest appear to be resolved. Our candidate galaxies have a median half-light radius of  $0.46 \text{ kpc}$ . The small circles denote the two objects where GALFIT did not converge; thus, we show the SE half-light radius.

## 6. Previously Identified $z \gtrsim 9$ Candidates in CEERS

### 6.1. Candidates Identified with HST

The area presently covered by CEERS covers two  $z \sim 9$ –10 galaxies previously identified by Finkelstein et al. (2022a), EGS\_z910\_40898 and EGS\_z910\_65860 (none of the candidate  $z \gtrsim 9$  galaxies from Bouwens et al. 2019 fall in this first

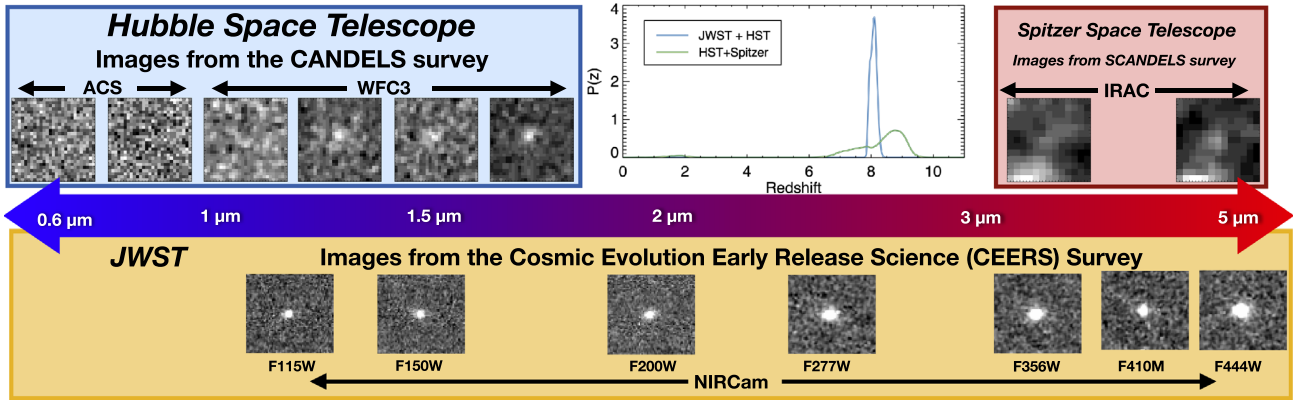


**Figure 9.** Candidate galaxy EGS\_z910\_40898, first published by Finkelstein et al. (2022a) as a  $z \sim 9$  galaxy candidate. This source was detectable by HST, albeit in only three filters and at only modest significance. Even in 50 hr of Spitzer/IRAC imaging, it was marginally detected. In just  $<3000$  s with JWST/CEERS, this source is extremely well detected in all seven NIRCcam filters, highlighting the power of JWST to probe the very early universe. In the top middle panel, we compare the previous  $\mathcal{P}(z)$  to that now possible with JWST, finding a much sharper peak centered at  $z \sim 8.1$  (the F115W–F150W color is only marginally red, implying a Ly $\alpha$  break at the blue edge of F115W).

epoch of CEERS NIRCcam imaging). In Figure 9, we show a comparison of the first object in NIRCcam versus HST and Spitzer imaging. While the object was only detected at modest significance in the  $\sim$ few-orbit HST imaging and barely at all in the 50 hr depth Spitzer/IRAC imaging, it is extremely well detected ( $S/N > 30$ ) in  $<3000$  s in all seven NIRCcam filters.

In this figure, we also compare constraints on the photometric redshift from the previous HST + Spitzer photometry of EGS\_z910\_40898 to the present JWST + HST photometry. While this object was previously selected as a  $z \sim 9$  candidate, as the majority of the  $\mathcal{P}(z)$  was at  $z \gtrsim 9$ , the primary peak extended down to  $z < 7$ , and there was a nonnegligible secondary peak at  $z \sim 2$ . With the significant improvement in photometric constraints, there is now a single narrow peak at  $z \sim 8.1$ . The best-fitting redshift is modestly lower than the previous value due to the only marginally red F115W–F150W color, implying that the Ly $\alpha$  break is toward the blue end of the F115W filter. Observations of this object highlight the capabilities of JWST to significantly improve constraints on photometric redshifts compared to the pre-JWST era.

The second object, EGS\_z910\_65860, however, shows no significant flux at all at the expected position (Figure 10). This implies that the source identified in the HST imaging was either spurious or a transient phenomenon. Finkelstein et al. (2022a) performed a detailed vetting process to remove all forms of spurious sources, including persistence; thus, this seems like an unlikely solution. We therefore consider whether the observations are consistent with a transient source. This object showed significant detections in HST F125W and F160W imaging, with no detections in F606W, F814W, F105W, or F140W. While 3D-HST F140W preimaging was shallower than the CANDELS imaging, it was curious that this object showed no detection, as its SED (anchored by F125W and F160W) should have been detectable.

We thus investigate the date of each of these observations. The F125W and F160W images were taken in 2013, with two images taken  $\sim 50$  days apart (April 2 and May 24). We made updated HST mosaics (following the procedure in Koekemoer et al. 2011) around the position of this source in each epoch separately, and we see a clear detection in both bands in both epochs. This further refutes the hypothesis that this disappearing source was spurious. Adding to the likelihood of a transient

explanation is that the source is fading between the two epochs, with the ratio of fluxes from the first to second epoch being 2.5 and 2.0 for F125W and F160W, respectively (fluxes were measured with SE on each epoch separately using MAG\_AUTO to approximate total fluxes). The nondetection of this source in F140W is easily explained, in the context of a transient interpretation, by the acquisition date of those images, which was 1.5 yr earlier than F125W and F160W (2011 December 2).

While the apparent Ly $\alpha$  break between F105W and F125W could imply that this object is a  $z \sim 9$  transient, the F105W imaging was obtained much later, on 2015 April 1. Likewise, the F606W images were taken in 2004 and 2011, while the F814W images were taken in 2004, 2011, and 2013. The SCANDELS Spitzer/IRAC imaging was obtained over many years from 2003 to 2012, but the bulk was obtained between 2010 and 2012 (Ashby et al. 2015). We therefore do not have the contemporaneous photometry needed for a reliable redshift of this source. What we do know is that the host galaxy is fainter than the limit of our NIRCcam imaging. Taking the limit of our deepest image in Table 2, we find that the observed flux in the first F160W epoch (23.6 nJy) is  $\sim 150$  times brighter than the  $1\sigma$  upper limit of our NIRCcam imaging. The compact morphology of this source, along with the lack of apparent proper motion between the two CANDELS epochs, leaves a supernova as the most likely explanation (a proper motion of less than the F160W PSF in 50 days indicates a distance of more than 1 pc, ruling out a solar system object). We show the observed fluxes/limits versus time in the left panel of Figure 10, while in the right panel, we show constraints on host galaxy absolute magnitude.

While nearly any redshift is plausible from a luminosity standpoint (from a low-redshift dwarf galaxy to a very high redshift  $\sim L^*$  galaxy), the significant fading over a 50 day time period argues against a very high redshift due to time dilation of the supernova decay curve. From the observed (sparse) light curve, we can only place loose constraints on the nature of the transient, following the methods of Rodney et al. (2014). The data favor classification as a core-collapse supernova with a redshift ranging from  $z \simeq 0.2$  to 1.2, with maximum likelihood at  $z \simeq 1.1$  and a slight preference for Type Ib/c supernovae

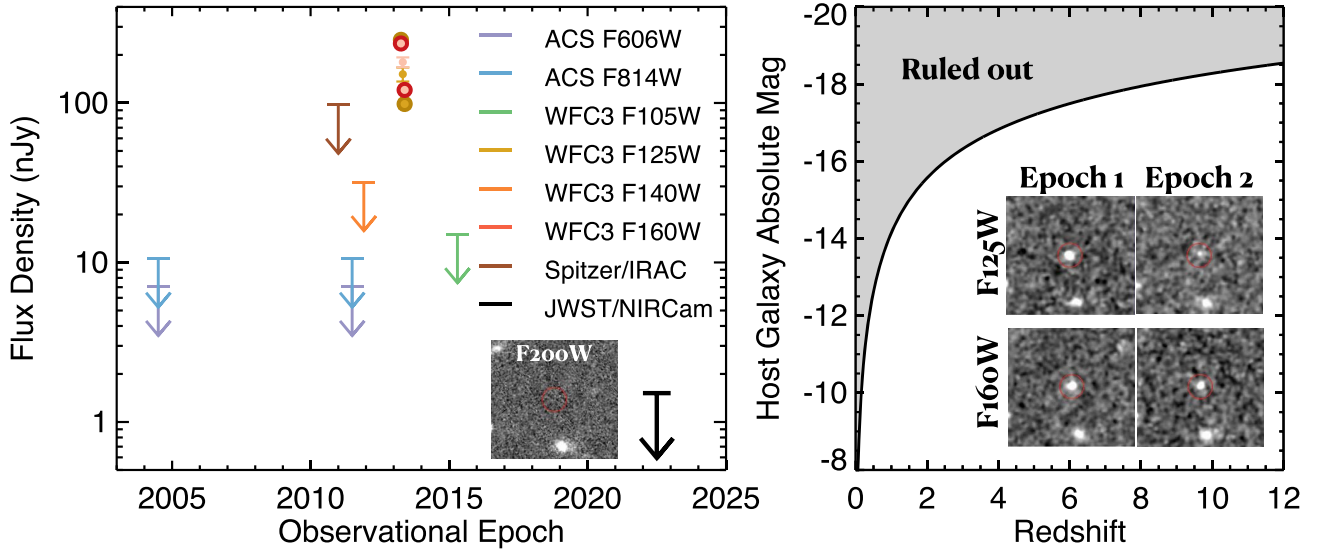


**Figure 10.** (Left) Flux vs. observational epoch for the object EGS\_z910\_68560, first published by Finkelstein et al. (2022a) as a  $z \sim 9$  galaxy candidate. The colors denote the filter. The small circles denote the integrated CANDELS F125W and F160W fluxes, while the larger circles denote the fluxes measured in each epoch, 50 days apart. The object is detected in both epochs in both bands, fading by a factor of  $\sim 2.5$  and  $2.0$  in F125W and F160W, respectively, across this time interval. The object is not detected in any of the CEERS imaging; the inset image shows this position in the CEERS F200W image. This implies that the object is  $>150\times$  fainter now than it was when it was detected. (Right) Limits on the host galaxy absolute magnitude, taken by applying the cosmological distance modulus to the CEERS upper limit. With the exception of the extremely low-redshift universe, a wide range of host galaxy absolute magnitudes are plausible, making it difficult to constrain the redshift of this supernova, though analysis of the light curve implies a likely redshift of  $z \sim 0.2\text{--}1.2$ . The inset panels show the images of this transient source in both CANDELS epochs in F125W and F160W.

over Type II. Nevertheless, the data are also compatible with Type Ia at  $z \simeq 1.45$ .

### 6.2. Candidates Identified with CEERS

At the time of this writing, there have been five previously submitted papers that have identified  $z \gtrsim 9$  candidates from these CEERS imaging data (D23; Finkelstein et al. 2022b; Harikane et al. 2023; Labbe et al. 2022; Whittler et al. 2023). In this section, we compare our current analysis to these previous results, noting that differences in selection techniques may bias the redshift ranges that a particular study is sensitive to. We also emphasize that while the selection of a candidate by more than one study does increase the confidence in the object’s fidelity, the presence or lack of a galaxy in a given sample is often easily attributable to differences in data reduction, photometric methodology, and selection criteria.

First, Finkelstein et al. (2022b) published a paper on a single galaxy, Maisie’s Galaxy, which they identified as a  $z \sim 12$  galaxy candidate. While they used the same full CEERS imaging data set as we use here (albeit with an earlier version of the data reduction), they employed highly conservative selection criteria to identify a single extremely robust galaxy candidate due to the nascent state of the data reduction pipeline and photometric calibration c. 2022 July. This object is in our galaxy sample, here known as CEERS2\_5429. Our photometric redshift constraints for this source are  $z_{\text{phot}} = 11.5^{+0.2}_{-0.6}$ . This is consistent at the  $\sim 1\sigma$  level with the value of  $z_{\text{phot}} = 11.8^{+0.3}_{-0.2}$  from Finkelstein et al. (2022b), with the small differences in the redshift attributable to small changes in photometry due to the updated photometric calibration now available.

The largest previous sample of high-redshift galaxies in the CEERS field comes from D23, who selected 19 high-redshift galaxies over the CEERS field. They required dropouts in the

F115W (or redder) bands to be selected, biasing the sample to  $z > 9.5$  (where  $\text{Ly}\alpha$  redshifts out of F115W). Here we compare to their revised sample (c. 2022 October). We find nine galaxies in common between our two samples. Of the 17 candidates in our sample but not in D23, 14 are at  $z \lesssim 9.5$ ; thus, their absence from the D23 sample is expected via their requirement of no significant flux in F115W. The remaining three candidates in our sample and not in D23, CEERS1\_1730, CEERS1\_7227, and CEER6\_4407, have  $z_{\text{best}} > 10$ ; thus, in principle, they could have been selected by D23. Of the nine sources in common, the median difference in the photometric redshifts is  $0.3 \pm 0.7$ , with all redshifts agreeing within  $\Delta z < 1$  (Figure 11), with the exception of our source CEERS6\_7641 (D23 ID 30585), which we find has  $z_{\text{best}} = 9.0$  compared to their value of  $z_{\text{best}} = 10.6$ . However, as shown in Figure 7, the  $\mathcal{P}(z)$  for this source is quite broad and contains a second peak at  $z \sim 10.4$ ; thus, our results are fully consistent with those of D23.

Of note is that our sample contains D23 object 93316 as object CEERS2\_2159, and our photometric redshift is nearly precisely equal to the D23 value of  $z = 16.4$ . This object is remarkably bright ( $m_{\text{F277W}} = 26.5$ ), and some evidence is present from both submillimeter imaging and environmental studies that indicate  $z \sim 5$  (Naidu et al. 2022a; Zavala et al. 2023). The JWST photometry alone very strongly prefers this ultrahigh redshift. Follow-up spectroscopy and millimeter interferometry will soon reveal the true nature of this potentially record-breaking system.

We next explore the properties of the 10 galaxies selected by D23 that are not in our final high-redshift galaxy sample. Of these 10, we find that five are faint enough that they did not meet our source detection significance criteria. Some of these are faint enough in our catalog that their photometric redshifts are not well constrained, while others show peaks at  $z > 10$ . Four more sources show primary peaks at  $z > 10$  but have

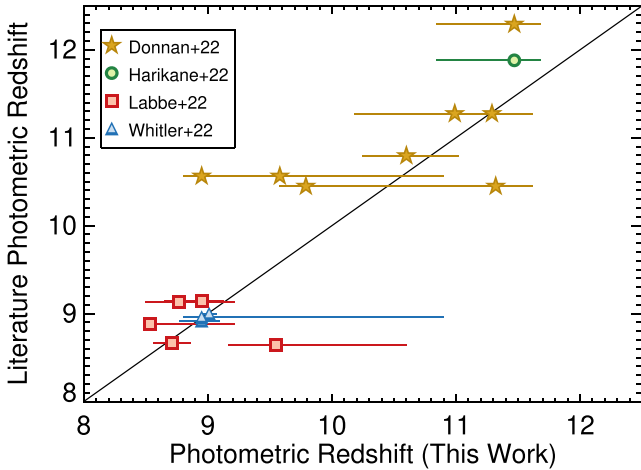


**Figure 11.** Comparison of our photometric redshifts to those for objects in our sample that were previously published as  $z > 8.5$  galaxy candidates from CEERS data in the literature, showing good agreement (not shown is the  $z \sim 16$  candidate, where the agreement is good between the three studies who have published it). As discussed in Section 6.2, for literature sources not present in our sample, we find in our catalog that they typically miss our detection significance and/or  $\Delta\chi^2$  criteria, though often the  $\mathcal{P}(z > 10)$  is nonzero.

secondary peaks at  $z < 4$  that are large enough for our selection criteria to remove these sources (these D23 IDs 1434\_2, 26409\_4, 5628\_2, and 6647 all have  $\Delta\chi^2 < 4$  in our catalog). For only one source, D23 ID 61486, do we find a strong low-redshift solution. This object exhibits a fairly flat SED in our catalog, though it exhibits a red F115W–F150W color, which could be indicative of a true  $z > 9$  Ly $\alpha$  break. Overall, we find strong consistency between objects in common in both our sample and that of D23, and for the D23 sources not in our sample, a high-redshift nature is possible given our photometry.

We next compare to Harikane et al. (2023). At the time of this writing, only the original sample, pre-photometric calibration update, was available for comparison. In the CEERS field, they selected galaxies as F150W or F200W dropouts, restricting their sample to  $z \gtrsim 12$  and selecting six high-redshift candidates. Of these six, two are in common with our sample: CEERS2\_5429 (Maisie’s Galaxy; Harikane ID CR2-z12-1) and CEERS2\_2159 (D23 93316; Harikane ID CR2-z17-1), with Harikane et al. having  $z_{\text{best}} = 11.88$  and 16.45 for these two objects, respectively. Of the four sources in their sample we do not recover, for CR2-z12-3, CR3-z12-1, and CR6-z12-1, our  $\mathcal{P}(z)$  shows a primary peak at  $z > 10$ , but the low-redshift peak is significant, with  $\Delta\chi^2 < 4$  for all three. All three sources are also faint and do not meet our detection significance criteria. For their source CR2-z12-1, we find  $z < 6$ , driven by an  $\sim 6\sigma$  detection in F115W, and a blue F115W–F150W color.

Labbe et al. (2022) selected candidate massive galaxies at  $7 < z < 11$  as those with detectable Ly $\alpha$  and Balmer breaks in their photometry. For this comparison, we use an updated sample made available following improvements in photometric calibration (I. Labbe 2022, private communication). Of their 13 sources, they reported photometric redshifts of  $> 8.5$  for five of them. Promisingly, all five of these sources are in our sample, with our Labbe et al. IDs of CEERS1\_3910 (39575), CEERS2\_1298 (21834), CEERS2\_2402 (16624), CEERS2\_7534 (14924), and CEERS3\_1748 (35300), with the best-

fitting photometric redshifts agreeing to  $\Delta z < 1$  (and  $\lesssim 0.3$  for 4/5).

Finally, Whilter et al. (2023) studied the stellar populations of bright galaxies at high redshift in CEERS. We compare to an updated sample, again following improved photometric calibration (L. Whilter 2022, private communication). In this sample, they have six galaxies with  $z_{\text{best}} > 8.5$ . Three of these sources are in our sample (CEERS1\_3858, CEERS1\_6059, and CEERS6\_7641, with Whilter et al. IDs of 37135, 37400, and 9711, respectively). The photometric redshifts for these three agree extremely well ( $\Delta z < 0.05$ ) with our estimates. Of the three sources we do not recover, we find a strong  $z \sim 10$  peak for their ID 7860; this source narrowly misses our sample with  $\Delta\chi^2 = 3.7$ . The ID 14506 does show a red F115W–F150W color, but our analysis prefers a 4000 Å break rather than a Ly $\alpha$  break, though a very small peak is present at  $z \sim 11$ . For ID 34362, a  $z \sim 9$  peak is dominant in our measurements, but  $\sim 50\%$  of the integrated  $\mathcal{P}(z)$  is contained in a  $z \sim 2$  peak.

In Figure 11, we compare the photometric redshifts from our study to these previous works for sources in common. As discussed above, especially considering the mix of photometric procedures and photometric redshift techniques, the agreement is generally good.

As one final comparison, we compare our estimated total magnitudes with the published magnitudes for those candidates in common (where, using the information available, we compare F200W for D23 and Whilter et al. 2023, F356W for Harikane et al. 2023, and F444W for Labbe et al. 2022). We find the largest discrepancy with D23, where for the nine sources in common, the median magnitude differences between our cataloged total magnitudes and those of D23 is  $-0.3$  mag (meaning that our fluxes are brighter); however, there is significant scatter, with one source being as much as 1 mag brighter in our catalog and another being 0.4 mag fainter in our catalog. Further exploring this discrepancy requires a deeper comparison between the procedures adopted to estimate total fluxes. Comparing to the other studies, we find results more in agreement. For the four sources in common with Whilter et al. (2023), the median magnitude offset is  $-0.1$ , with individual objects ranging from  $-0.2$  to zero. For the two objects in common with Harikane et al. (2023), our magnitudes are fainter by 0.1 and 0.3 mag. Finally, for the five sources in common with Labbe et al. (2022), our magnitudes are all fainter by 0.05–0.2 mag, with a median of 0.15 mag. We conclude that while there is significant scatter in the photometry due to the various processes used to reduce and analyze the data, we find no evidence that our photometry is significantly systematically shifted compared to other studies, especially by the large amount needed to explain the observed luminosity function excess (Section 7.1). Clearly, improving photometric agreement between different photometric catalogs is a key goal for the near future.

## 7. The Evolution of Galaxies in the First 500 Myr

Here we investigate what constraints we can place on galaxy evolution with our sample of 26 candidate  $z \sim 8.5$ –16.5 galaxies. While it is early in the JWST mission and the sample size is modest, the fact that our sample contains a large number of galaxies at  $z > 9$  allows us to investigate what constraints are possible. We first measure the rest-frame UV luminosity function at  $z \sim 11$  in comparison to both previous results and expectations from empirical extrapolations. We then compare

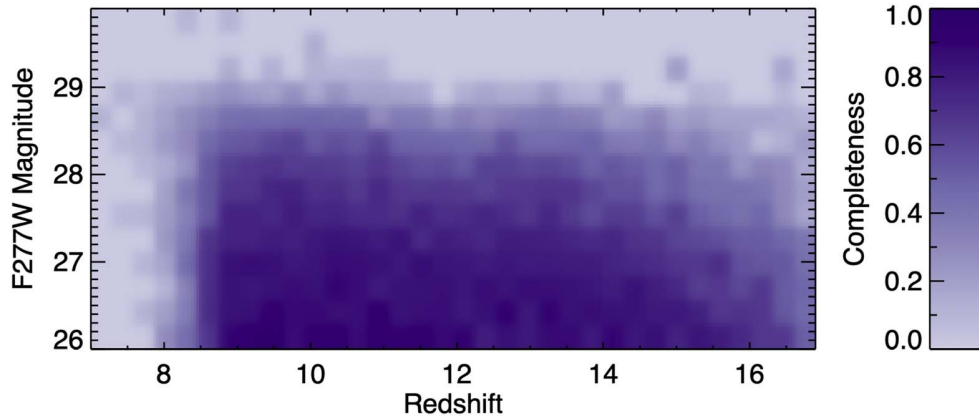


**Figure 12.** Total completeness as a function of input redshift and F277W apparent magnitude. These values were derived by simulations where we inject compact sources with realistic (modestly blue) SEDs into our imaging and attempt to recover them with our analysis pipeline. The shading denotes the fraction of sources in each bin of input redshift and magnitude, which were both detected by SE and satisfied our sample selection. The incompleteness at  $z < 8.5$  is expected via our sample selection. We see that the CEERS imaging allows recovery of galaxies across the entire redshift range of interest to very high completeness at  $m_{F277W} < 28.0$ , with the completeness dropping steadily from  $m = 28$  to 29.

the cumulative number of galaxies to predictions from a suite of theoretical models to explore the accuracy with which these models predicted galaxy abundances in this early epoch.

### 7.1. The $z \sim 11$ Rest-UV Luminosity Function

The UV luminosity distribution function is one of the key observational diagnostics of galaxy evolution in the early universe. With each technological leap leading to a new redshift era being observable, this quantity is always of immense interest (e.g., Bouwens et al. 2004; McLure et al. 2013; Finkelstein et al. 2015), as it is directly comparable to simulation predictions, helping to constrain the physical mechanisms regulating galaxy evolution. While the extensive amount of deep-field imaging data available from the full Cycle 1 data set will lead to excellent constraints on this quantity, here we gain a first look by exploring constraints placed by the CEERS data.

For this first-look luminosity function, we focus on the specific redshift range of  $z \sim 9.5\text{--}12$ . We exclude  $z = 8.5\text{--}9.5$  for two reasons. First, there is a likely overdensity at  $z = 8.7$  (e.g., Finkelstein et al. 2022a; Larson et al. 2022a) that would bias this quantity high. Second, at  $z > 9.5$ , the Ly $\alpha$  break is fully redward of F115W, providing a true JWST dropout sample that is not dependent on the shallower HST imaging. We choose the upper bound of  $z \sim 12$ , as only two galaxies in our sample have higher photometric redshifts.

To measure the UV luminosity function, we require an estimate of the effective volume over which we are sensitive to galaxies. This is a function of both redshift and source brightness and accounts for incompleteness due to both photometric measurements and sample selection. Following Finkelstein et al. (2022a), we estimate the completeness by injecting mock sources of known brightness into our images. We do this separately for each of the four fields, injecting  $10^3$  sources per iteration, with  $\sim 30$  iterations per field, to avoid crowding.

We generate source morphologies with GALFIT (Peng et al. 2002). While the completeness can depend sensitively on source size due to surface brightness dimming, our sources are quite compact (Figure 8); thus, we choose a lognormal half-light radius distribution such that the size distribution of the

recovered sources matches well that of our galaxy sample (noting that if there were highly extended sources not present in our sample, we would be underestimating the incompleteness). While we choose Sérsic profiles (with a lognormal distribution peaked at  $n = 1$ ), our size assumption results in a peak of unresolved sources, with a tail toward modestly resolved sources. We generate galaxy SEDs assuming a lognormal distribution in magnitude and a flat distribution in redshift using Bruzual & Charlot (2003) templates with stellar population properties tuned to generate fairly blue galaxies (this results in a median UV spectral slope ( $\beta$ ) of  $-2.3$ , with a tail to  $-3$  and  $-1$ ). We note that while we use a specific SPS model here, the completeness simulations are broadly dependent on the UV colors produced; thus, the completeness results would be broadly similar using a different SPS model provided the UV slope range was similar.

After sources are added to the images, the images are processed through our entire analysis pipeline in the same way as our real data, measuring photometry with SE, applying all aperture corrections (though we did not apply the small zero-point offsets, as those may be due to real instrumental offsets not captured in these simulations), measuring photometric redshifts with EAZY, and applying our sample selection. In Figure 12, we show our completeness as a function of input redshift and F277W magnitude. This highlights that our sample selection accurately begins to select galaxies at  $z \gtrsim 8.5$ . Our completeness remains high to  $m \sim 28.0$ , beginning to fall off at  $m > 28.5$ , consistent with prelaunch expectations.

To calculate rest-UV absolute magnitudes for both our real and simulated sources, we follow Finkelstein et al. (2015), performing a basic round of SED fitting and measuring  $M_{1500}$  from the bandpass-averaged flux over a top-hat bandpass spanning  $1450\text{--}1550 \text{ \AA}$  in the rest frame. We use  $10^3$  Monte Carlo simulations to obtain uncertainties on these magnitudes. For the completeness for our luminosity function estimate, we require the simulated sources to have best-fit photometric redshifts spanning  $9.5\text{--}12$ , to match those of our galaxy subsample. We then calculate our completeness as a function of absolute magnitude and measure effective volumes in bins of absolute magnitude by integrating over the comoving volume element multiplied by the completeness for a given magnitude

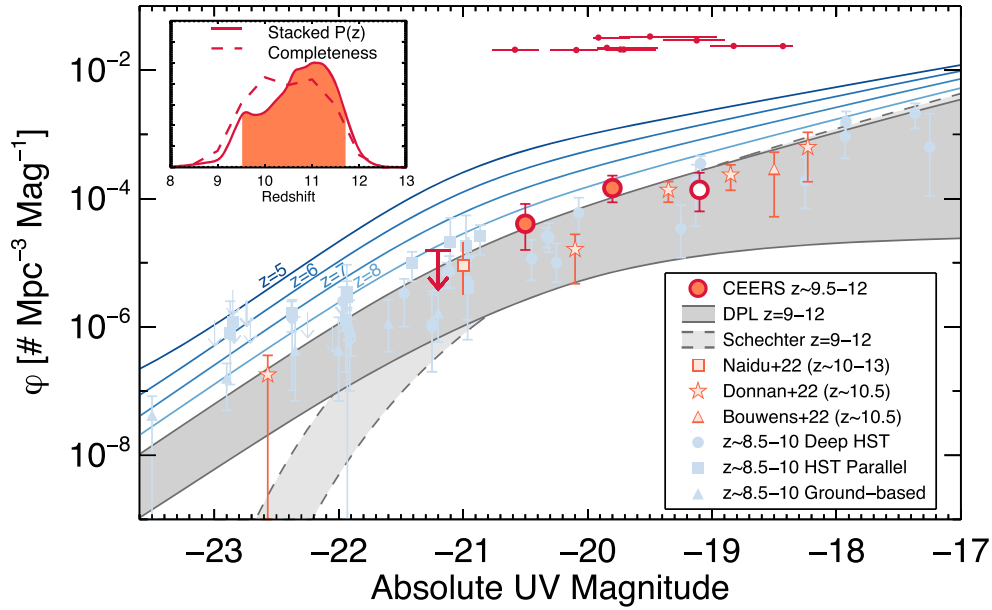


**Figure 13.** Rest-frame UV luminosity function at  $z \sim 11$ , shown as the red circles (the open circle denotes our faintest bin, where we are  $<30\%$  complete). Each galaxy’s magnitude and magnitude uncertainty are denoted by a small circle and line at the top of the figure. The light red symbols show literature constraints from JWST data from GLASS (Naidu et al. 2022b), CEERS+GLASS (D23, who also used UltraVISTA), and the HUDF (Bouwens et al. 2022b). The light blue points show a compilation of data from the literature at  $z \sim 9$ – $10$ . Circles denote results from studies that used (modestly) deep imaging from surveys such as CANDELS and the HFF, including McLeod et al. (2015), Oesch et al. (2018), and Bouwens et al. (2019, 2021). The squares denote studies making use of HST pure parallel surveys, including Bernard et al. (2016), Morishita et al. (2018), and Rojas-Ruiz et al. (2020). The triangles denote results from the wide-area ground-based studies of Stefanon et al. (2019) and Bowler et al. (2020). The blue lines show the predictions from the evolving DPL luminosity functions from Finkelstein & Bagley (2022) at  $z = 4$ – $8$  (this model was fit to data at  $z = 3$ – $9$ ). The dark gray shaded region shows the predictions from these DPL fits extrapolated to  $z = 9$  (upper bound)— $12$  (lower bound); the light gray shaded region (outlined with dashed lines) shows a similar extrapolation from the evolving Schechter function fits from Finkelstein (2016; this model was fit to data at  $z = 4$ – $8$ ). The inset shows the stacked  $\mathcal{P}(z)$  of the galaxies used in this luminosity function, as well as the redshift distribution estimated from the completeness simulations at  $M_{UV} = -20$ . The observed  $z \sim 11$  luminosity function is consistent with the top end of both smooth extrapolations, implying that the observed smoothly UV luminosity function evolution from  $z = 4$  to  $9$  may be slowing at  $z \sim 11$ .

**Table 3**  
 $z \sim 11$  UV Luminosity Function

$M_{1500}$ (mag)	Number of Galaxies	Effective Number	$\phi \times 10^{-5}$ ( $\text{Mpc}^{-3} \text{mag}^{-1}$ )	$V_{\text{eff}}$ ( $\text{Mpc}^3$ )
-21.2	0	$0.0 \pm 0.2$	$<2.8$	92,200
-20.5	1	$1.4 \pm 0.6$	$4.0^{+4.2}_{-2.5}$	74,300
-19.8	6	$4.8 \pm 1.0$	$14.6^{+8.2}_{-5.9}$	51,900
-19.1 <sup>a</sup>	2	$2.4 \pm 1.0$	$13.7^{+11.5}_{-7.4}$	30,600

**Notes.** The number densities are derived via an MCMC method that includes photometric uncertainties; thus, galaxies can contribute to the number density in more than one bin. The effective number column lists the mean and standard deviation of the number of galaxies per bin from these MCMC simulations, while the number column gives the actual value based on the measured magnitude.

<sup>a</sup> Our data are  $<30\%$  complete in this faintest bin, so we do not consider this value reliable; it is indicated as an open symbol in Figure 13.

and redshift over our current survey area of  $35.5 \text{ arcmin}^2$ . We list our effective volumes in Table 3.

We measure our luminosity function following the methodology of Finkelstein et al. (2015), adopting a bin size of  $0.7 \text{ mag}$ . The number density in each bin is estimated via Markov Chain Monte Carlo (MCMC; see details in Finkelstein et al. 2015), sampling galaxies’ absolute magnitude posterior distributions, such that galaxies can fractionally span multiple magnitude bins. We note that at  $M_{UV} > -19.5$ , our completeness falls below  $30\%$  of its maximum value; thus, our faintest bin is shaded in white to indicate that the value is dominated by the completeness correction.

In Figure 13, we show our luminosity function results. In the top left panel, we show the stacked  $\mathcal{P}(z)$  of the 10 sources in our sample at  $9.5 < z_{\text{best}} < 12.0$ . The FWHM of this normalized distribution spans  $z = 9.5$ – $11.7$ , with a peak at  $z \sim 11$ . The dashed line shows the completeness from our simulations as a function of redshift at the median absolute magnitude of our sample, which probes a broadly similar redshift range, albeit with a flatter distribution. In this figure, we also plot recent  $z \sim 11$  results from D23, Naidu et al. (2022b), and Bouwens et al. (2022a). While the numbers in all studies are fairly small, the agreement between all studies is encouraging. We also compare to a wealth of studies in the literature from HST at  $z = 8.5$ – $11$ .

Broadly speaking, our results at  $z \sim 11$  do not show significant evolution from these modestly lower redshifts. This is consistent with the conclusion from Bowler et al. (2020), who noted that the bright end of the UV luminosity function ( $M_{UV} = -22$  to  $-23$ ) shows little evolution from  $z = 8$ – $10$ . However, here we are beginning to probe fainter, yet we still see little evolution.

Finally, we comment on both the shape of the UV luminosity function and the overall evolution. In Figure 13, we plot two empirical extrapolations. The first is a Schechter function from Finkelstein (2016), who measured the evolution of the Schechter function parameters as a linear function of  $(1 + z)$  from  $z = 4$ – $8$ ; we plot this function evolved to  $z = 9$  and  $12$ , shown by the light gray shaded region. The dark gray shaded region is a similar empirical evolution, this time using data from  $z = 3$ – $9$  and assuming a double power-law (DPL) form from Finkelstein & Bagley (2022). Over the magnitude range